Optical constants of Pluto aerosol analogues from UV to near-IR

Lora Jovanovic, Thomas Gautier, Laurent Broch, Silvia Protopapa, Tanguy Bertrand, Pascal Rannou, Marie Fayolle, Eric Quirico, Luc Johann, Aotmane En Naciri, et al.

Optical constants of Pluto aerosol analogues from UV to near-IR

Lora Jovanović[1], Thomas Gautier[1], Laurent Broch[2], Silvia Protopapa[3], Tanguy Bertrand[4], Pascal Rannou[5], Marie Fayolle[6,7], Eric Quirico[6], Luc Johann[2], Aotmane En Naciri[2], Nathalie Carrasco[1]

[1] Université Paris-Saclay, UVSQ, CNRS, Sorbonne Université, LATMOS/IPSL, 78280 Guyancourt, France

[2] Université de Lorraine, LCP-A2MC, F-57000 Metz, France

[3] Southwest Research Institute, Boulder, CO 80302, USA

[4] NASA Ames Research Center, Moffet Field, CA 94035, USA

[5] GSMA, UMR 7331-GSMA, Université de Reims Champagne-Ardenne, 51687 Reims, France

[6] Université Grenoble Alpes, CNRS, IPAG, 38000 Grenoble, France

[7] Delft University of Technology, The Netherlands

Keywords

Pluto; Pluto, Aerosols, Haze; Pluto, Atmosphere; Pluto, Surface; Optical Constants

Abstract

Photochemical aerosols were detected as high as 350 km of altitude in Pluto's atmosphere during the *New Horizons* fly-by. These aerosols are thought to affect Pluto's climate, by acting as cooling agents, and the colours of Pluto's surface, in particular in the dark regions named Cthulhu and Krun and at the North Pole. Pluto atmospheric and surface models have so far used the optical constants of Titan aerosol analogues (tholins), whereas their chemical composition is known to differ from that of Pluto aerosol analogues.

In order to provide a new set of optical constants for Pluto tholins, we synthesized analogues of Pluto's aerosols and determined with spectroscopic ellipsometry their optical constants from 270 to 2100 nm. Three types of samples were produced from N_2:CH_4:CO gas mixtures differing

28 in their CH_4:N_2 mixing ratio, representative of different altitudes in Pluto's current atmosphere
29 or different seasons or epochs of Pluto.

30 Our analysis shows a strong absorption by Pluto tholins in the UV and visible spectral ranges,
31 with k index of a few 10^{-1} at 270 nm, in agreement with N- and O-bearing organic molecules.
32 Pluto tholins are less absorbent in the near-IR than in the UV-Vis wavelength range, with k of
33 a few 10^{-3} between 600 and 2100 nm. Our comparative study highlights the dependency of n
34 and k indices to the CH_4:N_2 mixing ratio. Aerosols formed at different altitudes in Pluto's
35 atmosphere or during different seasons or epochs of Pluto will therefore affect the budget of
36 Pluto radiative transfer differently.

37 The optical constants presented in this study were tested with a Pluto surface model and with a
38 model of light scattering. The surface modelling results highlight the suitability of these optical
39 constants to reproduce Pluto compositional observations in the visible spectral range by MVIC
40 and LEISA. The atmospheric modelling results conclude that Pluto tholins absorb 5 to 10 times
41 less than Titan tholins at 500 nm, and this lower absorption is consistent with Alice observations
42 of Pluto's haze.

43

44 **I.   Introduction**

45 Pluto fly-by by the *New Horizons* spacecraft on July 14th, 2015 evidenced the presence of
46 aerosols in Pluto's atmosphere by means of forward scattering observations and solar
47 occultations. These aerosols, accounting for 0.05-0.1 ppm$_V$ of the atmosphere, enshroud Pluto
48 and were detected at least as high as 350 km of altitude above the surface (Cheng et al. 2017;
49 Gladstone et al. 2016; Stern et al. 2015; Young et al. 2018).

50 Two mechanisms are currently proposed for the formation of hazes in Pluto's atmosphere.

51 The first one concerns the formation of aerosols through photochemistry, similar to what occurs
52 in Titan's upper atmosphere (*e.g.*, Gladstone et al. 2015, 2016; Wong et al. 2017; Young et al.
53 2018). Pluto's aerosols are thought to be formed by a complex photochemistry taking place in
54 the upper atmosphere, below 300 km and up to 900 km of altitude (Stern et al. 2018; Young et
55 al. 2018). This photochemistry is initiated by extreme-ultraviolet (EUV) sunlight and solar
56 Lyman-α photons. EUV radiation breaks the triple bonds of N_2 and CO in the upper atmosphere,
57 while Lyman-α photons – arriving directly from the Sun or scattered by the interplanetary
58 medium – breaks the C–H bonds in CH_4 at lower altitudes (Gladstone et al. 2015, 2016; Grundy

59 et al. 2018, and references therein), with a maximum CH_4 photolysis rate at 250 km of altitude

60 above the surface (Bertrand & Forget 2017). Pluto's photochemistry involves neutral and ionic

61 species created by the ionization and the dissociation of molecular nitrogen N_2, methane CH_4,

62 and carbon monoxide CO that constitute Pluto's atmosphere (Gladstone et al. 2016; Lellouch

63 et al. 2017; Young et al. 2018). This chemistry forms complex hydrocarbons, nitriles, and

64 oxygenated molecules, including some that can further polymerize and generate solid aerosols

65 (Krasnopolsky 2020; Wong et al. 2017).

66 The second mechanism, developed by Lavvas et al. (2020), would be different from that

67 proposed for Titan's hazes formation, due to the temperature difference between Pluto's and

68 Titan's upper atmospheres (~70 K versus ~150 K, respectively). This mechanism involves the

69 direct condensation of photochemical gases produced on Pluto, associated with a coating by

70 undersaturated light molecules (C_2 hydrocarbons) incorporated by heterogeneous processes

71 (possibly chemisorption or physisorption). This coating represents ~30% of the aerosol material

72 (Lavvas et al. 2020). These coated aerosols are then subject to a photon flux causing their

73 ageing, as studied in Carrasco et al. (2018) for Titan's aerosols.

74 Note that the present study focuses on Pluto's aerosols formed by photochemistry.

75 Questions remain regarding the size distribution of Pluto's haze particles since no single

76 solution can satisfy measurements from all instruments onboard *New Horizons*. Cheng et al.

77 (2017) pointed out the contradiction between haze brightness I/F profiles inferred from Alice

78 imaging spectrograph in the far-UV [52-187 nm] (Stern et al. 2008) and LORRI (LOng-Range

79 Reconnaissance Imager) panchromatic imaging instrument in the [350-850 nm] wavelength

80 range (Cheng et al. 2008). A model of Mie scattering by 0.5 µm spheres reproduces fairly well

81 the phase function of Pluto's haze at peak I/F measured in the visible by LORRI. However, this

82 Mie model gives UV extinction lower by an order of magnitude than that retrieved from Alice

83 solar occultation. On the opposite, results from a model of scattering by aggregates with bulk

84 radius of 0.15 µm composed of several thousands 0.01 µm spherical monomers agree with the

85 measurements made by Alice. They also match with the visible phase function measured by

86 LORRI, but only at higher altitudes in Pluto's atmosphere (Cheng et al. 2017). At higher

87 altitudes, Pluto's haze is thus thought to be mostly composed of aggregates of 0.15 µm particles

88 made up of 10 nm forward-scattering spheres. The haze particles present in the atmosphere

89 from the surface to ~15 km of altitude probably correspond to spherical particles that got larger

90 by direct condensation of photochemical products onto nuclei (Cheng et al. 2017; Gao et al.

91 2017; Gladstone et al. 2016; Lavvas et al. 2020; Stern et al. 2015; Young et al. 2018).

92   The haze particles are suspected to scatter the UV sunlight and to be the dominant factor of
93   extinction at wavelengths greater than ~150 nm, as the extinctions of hydrocarbons or nitriles
94   become less important with increasing wavelength. The haze particles thus contribute to the
95   spectrum of Pluto observed by the Alice instrument (Cheng et al. 2017; Steffl et al. 2020; Stern
96   et al. 2008). Pluto's aerosols are also expected to significantly absorb in the UV-Visible and in
97   the far-infrared spectral ranges and to be less absorbent in the near- and mid-IR (Grundy et al.
98   2018; Zhang et al. 2017; and references therein).

99   Recent numerical models have shown that these aerosols deeply affect Pluto's atmospheric
100 chemistry, for instance by depleting from the atmosphere small hydrocarbons that stick to the
101 negatively-charged aerosols, resulting in the formation of more complex ones (Krasnopolsky
102 2020; Luspay-Kuti et al. 2017; Wong et al. 2017). Pluto's climate is also affected by the
103 aerosols, that can serve as condensation nuclei (Gao et al. 2017; Lavvas et al. 2016; Luspay-
104 Kuti et al. 2017; Wong et al. 2017) or through direct radiative cooling of the atmosphere by the
105 absorption of solar radiations (Zhang et al. 2017). Pluto's atmosphere temperature, at ~400 km
106 of altitude, is around 30-40 K colder than model predictions for an atmosphere in radiative-
107 conductive equilibrium without haze (Gladstone et al. 2016; Zhang et al. 2017; Zhu et al. 2014).
108 Zhang et al. (2017) suggested this cooling to be due to the haze particles and their optical
109 properties. Due to a lack of both observational and experimental data on these optical properties,
110 the study by Zhang et al. (2017) was done using those of Titan aerosol analogues (Titan tholins)
111 produced on Earth. In addition, these photochemical aerosols have been suggested to account
112 for all of Pluto's colours at large scales, from the dark red colour of Cthulhu and Krun Maculae
113 to the yellow hue on Pluto's North Pole (Lowell Regio) (Grundy et al. 2018; Protopapa et al.
114 2017, 2020). The modelling studies of Pluto *New Horizons* data across the full [0.4-2.5 µm]
115 wavelength range by Protopapa et al. (2020) used optical constants determined for Titan tholins
116 by Khare et al. (1984) and Tran et al. (2003), given the lack of optical constants for Pluto tholins.
117 To explain the different colours on Pluto's surface, Grundy et al. (2018) used multiple-
118 scattering radiative transfer models with optical constants determined for Titan tholins by
119 several groups: Khare et al. (1984), Ramírez et al. (2002), Imanaka et al. (2004), Vuitton et al.
120 (2009), and Sciamma-O'Brien et al. (2012).

121 Protopapa et al. (2020) pointed out the lack of optical constants for tholins in the Vis-near-IR
122 wavelength range. Additionally, Zhang et al. (2017) highlighted that the optical constants
123 determined for Titan aerosol analogues strongly vary with the mode of production and that the
124 optical constants of Pluto's aerosols may be very different from those of Titan tholins. Note

125   that the review by Brassé et al. (2015) discusses the different optical constants determined for

126   Titan tholins.

127   Thus, to update and better constrain Pluto atmospheric models and to model Pluto's surface

128   spectra, the determination of the optical constants of Pluto aerosol analogues is strongly needed.

129   The aim of our work is to fill this gap, by providing optical constants of Pluto tholins from 270

130   to 2100 nm.

131   **II.   Experimental setup and protocol**

132   **1.   Production of Pluto aerosol analogues**

133   Following the protocol detailed in Jovanović et al. (2020), we used the experimental setup

134   PAMPRE (Production d'Aérosols en Microgravité par Plasma REactif) (Alcouffe et al. 2010;

135   Szopa, Cernogora et al. 2006), a cold plasma discharge to simulate the chemistry occurring in

136   Pluto's atmosphere and produce analogues of Pluto's aerosols. The gas mixture flows through

137   a cylindrical metallic grounded cage. Square silicon wafers of 1 cm^2 were placed at the bottom

138   of the cage. When the plasma is switched on, tholins form as thin films onto the silicon wafers.

139   Note that the optical constants of tholins are highly dependent on the experimental conditions

140   of synthesis and measurements (Brassé et al. 2015; Zhang et al. 2017). For readers interested in

141   the effect of using a UV lamp rather than a plasma discharge to synthesize tholins, we

142   recommend reading the review by Cable et al. (2012). In summary, tholins formed by UV

143   photochemistry in the laboratory tend to be less rich in N-bearing compounds, since UV lamps

144   cannot mobilize nitrogen chemistry. Indeed, lamp windows cut off UV wavelengths below

145   ~115 nm, which prevents direct dissociation of N_2, unlike what happens in natural atmospheres.

146   On the contrary, plasma setups such as PAMPRE tend to enhance nitrogen inclusion a bit too

147   much. The electron energy distribution in PAMPRE mimics well at first order the one of solar

148   photons (Szopa, Cernogora et al. 2006). However, a small difference is due to the slightly more

149   energetic tail of the Maxwellian energy distribution of the electrons in the plasma compared to

150   the Planck energy distribution of solar photons. This slightly higher population of electrons

151   induces a small bias due to over-dissociation of N_2, that is well known and has been extensively

152   studied regarding the tholins chemical composition. Since nitrogenous compounds tend to be

153   more absorbent, one could expect that tholins synthesized in laboratory by UV photochemistry

154   would probably be less absorbent in the UV-Vis spectral range, due to a poorer content in N-

155   bearing compounds. Where actual Pluto's aerosols would stand in that range is currently

156   unknown (as for Titan's aerosols), which is why we strongly encourage any other experimental

157 teams with similar facilities to perform studies similar to ours to extend the range of possible
158 laboratory data on this point.

159 Three types of tholins were synthesized in this work, from gas mixtures composed of various
160 N_2 (*Air Liquide*, ALPHAGAZ™ 2) and CH_4 (*Air Liquide*, CRYSTAL mixture) percentages
161 and a fixed CO (*Air Liquide*, CRYSTAL mixture) amount of 500 ppm (see Table 1), at
162 0.9 ± 0.1 mbar and ambient temperature. For readers interested in the effect of synthesis
163 temperature on aerosol analogues optical constants, we recommend reading Mahjoub et al.
164 (2014) who studied this effect for Titan tholins. In the present work, experiments were
165 performed at ambient temperature to avoid heterogeneous chemistry effects as described in
166 Mahjoub et al. (2014).

167 The CO atmospheric mole fraction of 515 ± 40 ppm (Lellouch et al. 2017; Young et al. 2018)
168 is not expected to vary much over time and space. This is due to the volatility of CO being close
169 to that of N_2 and the absence of CO-rich ice deposits on Pluto's surface (Bertrand & Forget
170 2016). The first type of tholins was produced in a gas mixture composed of $N_2:CH_4:CO$ at
171 99.5%:0.5%:500ppm – we will thereafter call this material "P_H". Given that the CH_4 mixing
172 ratio was found to be ~0.3% below 350 km of altitude (Young et al. 2018), P_H is relevant to the
173 composition of Pluto's atmosphere as observed in 2015 below 350 km of altitude above the
174 surface. The second tholins sample was produced in a gas mixture containing $N_2:CH_4:CO$ at
175 99%:1%:500ppm, mimicking Pluto's atmosphere at around 400 km of altitude above the
176 surface – thereafter called "P_{400}". The third one was produced in a gas mixture made of
177 $N_2:CH_4:CO$ at 95%:5%:500ppm, representative of Pluto's atmosphere between 600 and
178 700 km of altitude – thereafter called "P_{650}" (Lellouch et al., 2017, Young et al., 2018).

179 We note that the mean CH_4 atmospheric mixing ratio is predicted to vary from 0.01% to 5%
180 over annual or astronomical timescales (Bertrand et al. 2019; Bertrand & Forget 2016). The
181 tholins synthesized in the present work could therefore also serve as analogues for haze particles
182 produced during past epochs or different seasons of Pluto, with implications to its past and
183 future climates.

184 For the three types of tholins, the plasma ran for 90 minutes, forming films with thicknesses no
185 more than 1 µm (see Table 1) to ensure the validity of the spectroscopic ellipsometry technique
186 for the measurements (Fujiwara 2007; Mahjoub et al. 2012; Sciamma-O'Brien et al. 2012).

187

188 Table 1: Table presenting the three types of Pluto aerosol analogues analysed in this study.

Composition of the reactive mixture			Corresponding altitude above the surface on Pluto	Acronym of the aerosol analogues	Thickness of the thin film
N_2	CH_4	CO			
99.5%	0.5%	500 ppm	< 350 km	P_H	549.8 ± 0.6 nm
99%	1%	500 ppm	~ 400 km	P_{400}	540.9 ± 0.2 nm
95%	5%	500 ppm	600-700 km	P_{650}	651.0 ± 0.7 nm

189

190   The thickness of the thin films was determined by spectroscopic ellipsometry with a modified
191   Tauc-Lorentz dispersion model, as detailed below. We note that for the same synthesis duration,
192   the thin-film thickness increases when the amount of CH_4 injected in the reactive gas mixture
193   increases significantly, as discussed by Mahjoub et al. (2012).

194   **2. Spectroscopic ellipsometry**

195   The tholins thin films were analysed by spectroscopic ellipsometry. Using this analysis
196   technique, it is possible to determine the thickness of the tholins thin films, as well as their
197   optical constants n and k, the real and imaginary parts respectively of the complex refractive
198   index.

199   Spectroscopic ellipsometry measures the change in the polarization state between incident and
200   reflected light on the sample (the reader is referred to *e.g.,* Azzam & Bashara (1977), Tompkins
201   & Irene (2005) and Fujiwara (2007) for complete information on spectroscopic ellipsometry
202   technique). Incident light is linearly polarized, while reflected light is elliptically polarized.
203   The measured values are the ellipsometric parameters Ψ and Δ, related to the ratio of the Fresnel
204   amplitude reflection coefficients of the sample by fundamental equation:

205

206   $$r_p/r_s = \tan\psi\, e^{i\Delta} \quad (1)$$

207

208   for p- and s-polarized light[1] with the electric field in the plane of incidence and perpendicular
209   to the plane of incidence, respectively.

---

[1] r_p is the reflection coefficient of the sample for a polarization parallel to the plane of incidence ("p" for parallel) and r_s is the reflection coefficient of the sample for a polarization perpendicular to the plane of incidence ("s" for perpendicular, "senkrecht" in German).

Variable Angle Spectroscopic Ellipsometry (VASE) measurements were carried out using a phase-modulated spectroscopic ellipsometer (UVISEL, *Horiba Jobin Yvon*), equipped with a 150 W Xenon light source. Corresponding ellipsometric parameters were obtained through $(I_s(\lambda), I_c(\lambda))$ in the spectral range [270-2100 nm] with 5 nm steps according an integration time of 1000 ms, where $I_s = \sin(2\Psi)\sin(\Delta)$ and $I_c = \sin(2\Psi)\cos(\Delta)$, respectively. All measurements were performed for incidence angles between 60 and 75 degrees with 5° steps. By way of comparison, the ellipsometric analyses performed on Titan tholins thin films by Mahjoub et al. (2012, 2014) and Sciamma-O'Brien et al. (2012) were conducted for a single incidence angle of 70°.

The parameters of the optical model were adjusted by minimizing the Mean Square Error (MSE) defined as:

$$MSE = \frac{1}{N-1}\sum_{i=1}^{N}\left[\left(I_{s,i}^{calc}(\lambda) - I_{s,i}^{exp}(\lambda)\right)^2 + (I_{c,i}^{calc}(\lambda) - I_{c,i}^{exp}(\lambda))^2\right] \qquad (2)$$

where *calc* stands for the calculated and *exp* for the experimental values of (I_s, I_c) and *N* the number of experimental data $(I_s(\lambda), I_c(\lambda))$.

DeltaPsi2® software[2] was used to fit ellipsometric data.

The inversion of ellipsometric data was performed using a model of the sample [Si substrate / Tholins layer / Roughness layer / Air] as schematized in Figure 1.
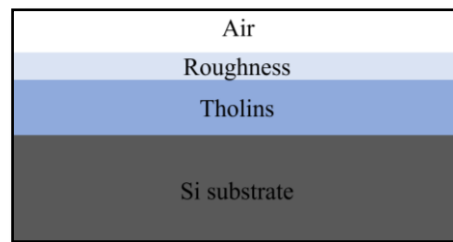

Figure 1: Scheme of the model of the samples analysed by spectroscopic ellipsometry.

In this model, the thickness of the roughness layer, the thickness of the tholins layer, and the dielectric function of the tholins layer were unknown, while the roughness layer was modelled by a mixture of 50% air and 50% tholins, according to Bruggeman Effective Medium Approximation (BEMA) (Bruggeman 1935).

---

[2] DeltaPsi2® software: https://www.horiba.com/en_en/products/detail/action/show/Product/deltapsi2-software-1648/

237 ### 3. Determination of the optical constants of Pluto tholins with two different inversion
238 ### methods: modified Tauc-Lorentz and "wavelength-by-wavelength" (λ-by-λ)

239 Spectroscopic ellipsometry is an indirect technique for determination of the sample physical
240 properties (*i.e.* thickness and optical constants). Using a model to describe the ellipsometric
241 response of the sample by adjusting specific fit parameters is thus necessary. Basically, the
242 model calculates the reflection coefficients r_p and r_s to retrieve the measured ellipsometric
243 parameters Ψ and Δ. An equation system for each wavelength λ is generated: Ψ = f (n, k, t) and
244 Δ = g (n, k, t), with $n(\lambda)$ and $k(\lambda)$ the real and imaginary parts respectively of the complex
245 refractive index, and *t* the thickness of the tholins thin film. The thickness *t* of the thin film and
246 the *n* index are initially determined in a transparent region of the thin film. Then, the fixed *t*-
247 value is used as an input parameter to determine *n* and *k* indices in an absorbing region of the
248 thin film. The inversion method, based on the natures of the analysed material and the
249 underlying substrate, is used to calculate *n* and *k* indices of the material for each wavelength.

250 In this work, we used sequentially two types of inversion method: modified Tauc-Lorentz
251 dispersion model to find the proper estimates of the initialization parameters, and "wavelength-
252 by-wavelength" (λ-by-λ) numerical inversion to determine precisely the optical constants *n* and
253 *k* of the tholins material.

254 ### a. Determination of the thickness and the optical constants of Pluto tholins by a
255 ### modified Tauc-Lorentz dispersion model

256 The first model we used is a Tauc-Lorentz dispersion model, based on the Tauc joint density of
257 states and the Lorentz oscillator, which was developed by Jellison and Modine (1996). This
258 dispersion model was developed to better describe the optical properties of semiconductor and
259 amorphous materials. This fitting model is thus adapted for tholins produced with the PAMPRE
260 experimental setup, as Hadamcik et al. (2009) observed these samples with Scanning Electron
261 Microscopy and showed that they present an amorphous structure.

262 In this model, the imaginary part $\varepsilon_{i,\mathrm{TL}}$ of the complex relative dielectric constant is given by the
263 product of the imaginary part of Tauc's dielectric constant $\varepsilon_{i,\mathrm{T}}$ (Tauc et al. 1966) with a
264 Lorentzian oscillator $\varepsilon_{i,\mathrm{L}}$:

265
$$\varepsilon_{i,\mathrm{TL}}(\mathrm{E}) = \varepsilon_{i,\mathrm{T}} \times \varepsilon_{i,\mathrm{L}} = \begin{cases} \dfrac{1}{\mathrm{E}} \dfrac{A E_0 C (\mathrm{E}-\mathrm{E_g})^2}{(\mathrm{E}^2-\mathrm{E}_0^2)^2 + C^2 \mathrm{E}^2} & \text{for } \mathrm{E} > \mathrm{E_g} \\ 0 & \text{for } \mathrm{E} \leq \mathrm{E_g} \end{cases} \quad (3)$$

266   where E (in eV) is the photon energy; E_g (in eV) is the optical bandgap energy specifying at
267   which energy the material becomes absorbent; E_0 (in eV) is the energy of the major absorption
268   peak in the UV (the Lorentz peak) $(E_g < E_0)$; A is the oscillator amplitude; and C is the
269   broadening term.

270   The real part $\varepsilon_{r,TL}$ of the complex relative dielectric constant is derived from the expression of
271     $\varepsilon_{i,TL}$ (Equation (3)) using the Kramers-Kronig integration (Kramers 1927; Kronig 1926):

272
$$\varepsilon_{r,\text{TL}}(\text{E}) = \varepsilon_{\infty} + \frac{2}{\pi} \cdot \text{P} \cdot \int_{\text{E}_g}^{\infty} \frac{\xi \cdot \varepsilon_{i,\text{TL}}(\xi)}{\xi^2 - \text{E}^2} d\xi \qquad (4)$$

273   where ε_{∞} is the high-frequency real dielectric constant; and P is the Cauchy principal value.

274   The optical constants *n* and *k* are then deduced from the real and imaginary parts of the complex
275   relative dielectric constant (Equations (3) and (4)) by the relation:

276
$$\varepsilon_{r,\text{TL}} + i \times \varepsilon_{i,\text{TL}} = (n + i \times k)^2 \quad (5)$$

277   In the standard Tauc-Lorentz model, the imaginary part *k* of the complex refractive index
278   becomes null for energies below the bandgap energy. This is due to the resolution of Kramers-
279   Kronig equations, but not to the intrinsic material properties. However, this *k* index is necessary
280   for numerical models (*e.g.*, radiative transfer, albedo, surface composition, haze vertical
281   profile).

282   To overcome this problem, we modified the standard Tauc-Lorentz model by adding oscillators
283   characterized by ε_{osc}:

284
$$\varepsilon_{\text{osc}} = \frac{f_j w_{0j}^2}{w_{0j}^2 - w^2 + i\gamma_j w} \qquad (6)$$

285   where ε_{osc} is the dielectric function; *w* is the light pulsation; f_j is the oscillator strength of the
286   j^{th} resonator; w_{0j} is the natural pulsation of the jth resonator; and γ_j is the damping rate of the
287   j^{th} resonator (friction coefficient).

288   Oscillators were added one by one to the model at different wavelengths, until the addition of
289   an additional oscillator had no longer significant improvement in the MSE (Equation (2)). In
290   this work, although the modified Tauc-Lorentz model was adapted for the determination of the
291   thin-films thickness, the addition of oscillators was not sufficient to retrieve *k* indices below the
292   bandgap energy (see Figure 3).

293

b. Determination of the optical constants of Pluto tholins by a "λ-by-λ" numerical
inversion method

296   Once the thickness of the thin films and the initial couples [n_{270nm}, k_{270nm}] characterized by the

297   modified Tauc-Lorentz dispersion model (values used as input parameters), we used the "λ-by-

298   λ" numerical inversion method to determine the optical constants of Pluto tholins.

299   In the "λ-by-λ" inversion method (also known as "direct data inversion" or "exact numerical

300   inversion"), *n* and *k* indices are calculated for each wavelength by applying mathematical

301   inversion of the Equation (1) (Fujiwara 2007). Theoretical ellipsometric parameters are

302   calculated (Ψ_{calc} and Δ_{calc}) and the values are compared to the experimentally measured

303   ellipsometric parameters (Ψ_{exp} and Δ_{exp}). A linear regression algorithm introduces for the initial

304   couple [n_{270nm}, k_{270nm}] the corrections needed to match (Ψ_{calc}, Δ_{calc}) and (Ψ_{exp}, Δ_{exp}). Then, the

305   process is applied iteratively over the whole spectral range (from 270 to 2100 nm): the values

306   for the couple [n_{λ}, k_{λ}] are calculated from the values of the couple [$n_{\lambda-\delta\lambda}$, $k_{\lambda-\delta\lambda}$] with δλ the

307   wavelength step between two measurements (here, 5 nm) (Fujiwara 2007; Keita et al. 2010;

308   Likhachev et al. 2015).

309   The "λ-by-λ" numerical inversion method gives a mathematical solution for [n_{λ}, k_{λ}] couples

310   from measured ellipsometric parameters Ψ and Δ, disregarding the *n* and *k* dependency on each

311   other at different wavelengths. For this procedure, other parameters, such as the thickness of

312   the thin film, and the optical properties of the underlying silicon substrate and the overlying

313   roughness layer, need to be accurately known, otherwise it can lead to multiple solutions,

314   unphysical dispersion or discontinuities in the optical constants, generally present at lower

315   energies in the inversion spectrum (Fujiwara 2007; Keita et al. 2010; Likhachev et al. 2015).

316   **c. Procedure to determine the optical constants *n* and *k* of Pluto tholins**

317   In summary, modified Tauc-Lorentz dispersion model is used to extract both thickness and

318   optical constants *n* and *k* by fitting the thickness values and the Tauc-Lorentz parameters. "λ-

319   by-λ" numerical inversion enables an exact modelling of the optical constants *n* and *k* in spectral

320   ranges where the fit is difficult with dispersion formulas and to check the optical constants

321   results obtained by dispersion formulas (modified Tauc-Lorentz in this work). A "λ-by-λ" fit

322   of the experimental data is performed on the only unknown optical constants *n* and *k* of the thin

323   film without fitting any parameter. To use this numerical inversion method, all parameters of

324   the optical model, such as thicknesses, must be known, which is not the case for tholins material

325   and thus induces much larger uncertainties. This method requires a (even rough) knowledge of

326 the order of magnitude of *n* and *k* indices for initialization. We thus used a two-pronged

327 approach, where the modified Tauc-Lorentz dispersion model is used to determine the

328 initialization parameters of the "λ-by-λ" numerical inversion method, which in return gives us

329 the optical properties with much higher confidence. Therefore, our procedure, based on two

330 sequential modified Tauc-Lorentz and "λ-by-λ" methods, is a good way to determine correctly

331 the optical constants *n* and *k* of the original sample system when the optical responses are not

332 available in the literature. The reader is referred to Keita et al. (2010) for more details about

333 these two methods.

III.   Results: Optical constants of Pluto aerosol analogues

335 Figures 2 and 3 respectively display the real and imaginary parts *n* and *k* of the complex

336 refractive index determined for P_H sample with a modified Tauc-Lorentz dispersion model (in

337 turquoise blue) and with a "λ-by-λ" numerical inversion method (in dark blue). The 2σ error

338 bars determined for the "λ-by-λ" inversion method (see Table SI.4 in Supplementary

339 Information) were calculated based on the uncertainties of I_s^{exp} and I_c^{exp} at different

340 wavelengths. The uncertainties were then linearly interpolated between two error bars in order

341 to obtain an envelope of uncertainty (in light blue). Note that these error bars do not include all

342 the uncertainties on *n*- and *k*-values. Indeed, the uncertainties on the raw   ellipsometric

343 measurements before modelling are known and are modest, given the quality of the setting of

344 the analytical instrument; these uncertainties are therefore not included in the error bars

345 presented. The major source of uncertainties corresponds to the inversion model used, including

346 *e.g.,* the number of fitting parameters and of oscillators used, the problem of presence of local

347 minima during the fit, and in particular the absence of initial values for the inversion. We can

348 nevertheless expect that the actual uncertainties on the optical constants of Pluto tholins would

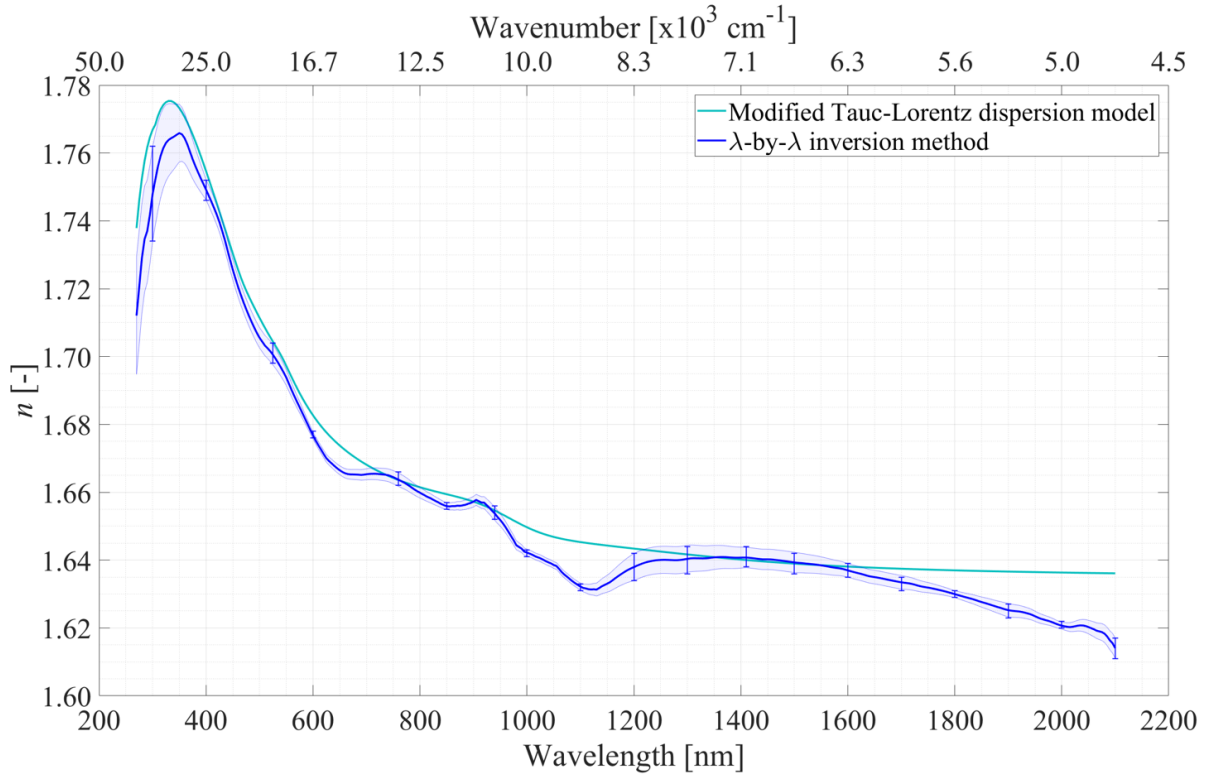349 be slightly higher than those presented here.

350

Figure 2: Real part *n* of the complex refractive index of Pluto aerosol analogues P_H determined by spectroscopic ellipsometry with a modified Tauc-Lorentz dispersion model (in turquoise blue) and with a "λ-by-λ" numerical inversion method (in dark blue). The 2σ error bars were experimentally determined for the "λ-by-λ" inversion method at different wavelengths. The uncertainties were then linearly interpolated between two error bars in order to obtain the envelope of 2σ uncertainty (in light blue).
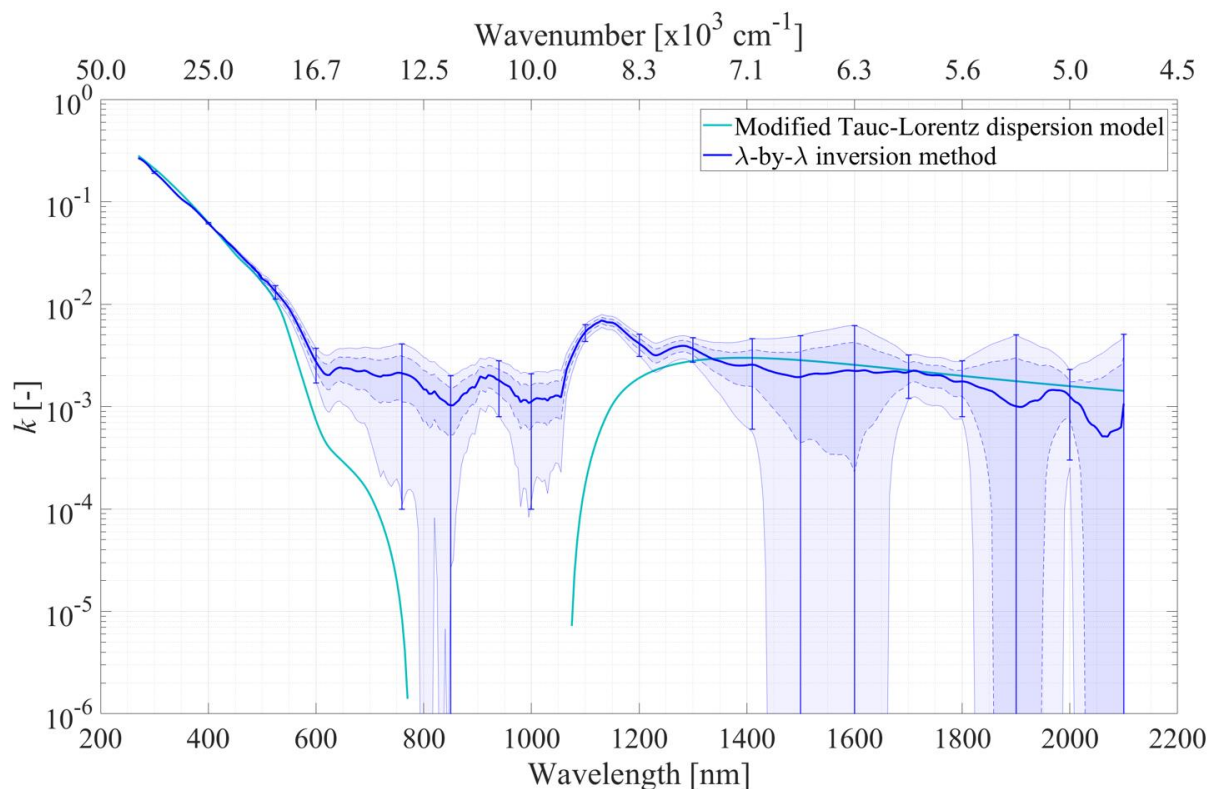
356

357

358

359 Figure 3: Imaginary part k of the complex refractive index of Pluto aerosol analogues P_H determined by
360 spectroscopic ellipsometry with a modified Tauc-Lorentz dispersion model (in turquoise blue) and with
361 a "λ-by-λ" numerical inversion method (in dark blue). The 2σ error bars were experimentally determined
362 for the "λ-by-λ" inversion method at different wavelengths. The uncertainties were then linearly
363 interpolated between two error bars in order to obtain the envelope of 2σ uncertainty (in light blue). The
364 envelope determined by dashed lines corresponds to 1σ uncertainty. Note that the y-axis was cropped at
365 10^{-6}, while the 2σ uncertainties of k-values reach 0 in the [800-850], [1450-1650] and [1820-2100] nm
366 regions.

367 In Figure 2, the dark-blue and turquoise-blue curves present the same profile, with a maximal
368 n-value of about 1.77 at 325-330 nm and decreasing values of n index between 330 and
369 2100 nm. In Figure 3, k-values determined with the two models are very similar in the [270-
370 490] and [1150-2100] nm regions. The dark-blue and turquoise-blue curves share the same
371 slope, indicating similar values for the bandgap energy (also called "absorption edge", *i.e.* the
372 wavelength at which there is a sharp increase of the k index). The bandgap energy determined
373 with the modified Tauc-Lorentz dispersion model (turquoise-blue curve) is around 575 nm,
374 while it is around 595 nm with the "λ-by-λ" numerical inversion method (dark-blue curve).
375 Beyond the bandgap energy, the behaviour of the k indices is the same, reaching an asymptotic
376 value of $\sim 2 \times 10^{-3}$ between 600 and 2100 nm.

377 From Figures 2 and 3, we can conclude that the choice of the fitting model – modified Tauc-
378 Lorentz or "λ-by-λ" – has no significant impact on the n and k indices determined for P_H sample
379 in the [270-600] and [1150-2100] nm regions. Each method has advantages and drawbacks
380 (specified in Sections II.3.a, II.3.b, and II.3.c). In this work, while the modified Tauc-Lorentz
381 dispersion model was adapted for the determination of the thin-films thickness, it could not
382 manage to determine non-null values for k indices between 740 and 1105 nm. This is due to the
383 software used, which cannot compute k-values below 10^{-4}. Therefore, we list in Tables SI.1,
384 SI.2 and SI.3 (found in Supplementary Information) the optical constants of Pluto aerosol
385 analogues P_H, P_{400} and P_{650} obtained by spectroscopic ellipsometry and determined with the "λ-
386 by-λ" fitting method from 270 to 2100 nm with a 5 nm increment. Note that n and k indices
387 presented in all the figures of the manuscript and listed in Tables SI.1-3 were smoothed by a
388 moving mean with a step of 15 data points. All the subsequent figures display the smoothed
389 optical constants determined with the "λ-by-λ" numerical inversion method.

**IV.   Impact of the altitude (or epoch) of aerosol formation on the optical constants and
         implications for radiative transfer**

392 P_H, P_{400} and P_{650} samples were produced with different N_2:CH_4:CO ratios. As CH_4 mixing ratio
393 strongly varies throughout the atmospheric column (Young et al. 2018), the purpose of
394 comparing these three samples is to determine if the altitude of formation of the aerosols in
395 Pluto's atmosphere has an impact on their optical constants.

1.   Effect on real part n of the complex refractive index

397 Figures 4 shows the real part n of the complex refractive index of P_H, P_{400} and P_{650} samples as
398 a function of wavelength. In this figure, the blue curve corresponds to P_H sample, the red curve
399 to P_{400} sample and the green curve to P_{650} sample. The 2σ error bars (see Table SI.4 in
400 Supplementary Information) were calculated based on the uncertainties of I_s^{exp} and I_c^{exp} for
401 different wavelengths. The uncertainties were then linearly interpolated between two error bars
402 in order to obtain the envelopes of uncertainty (in light blue, light red and light green).
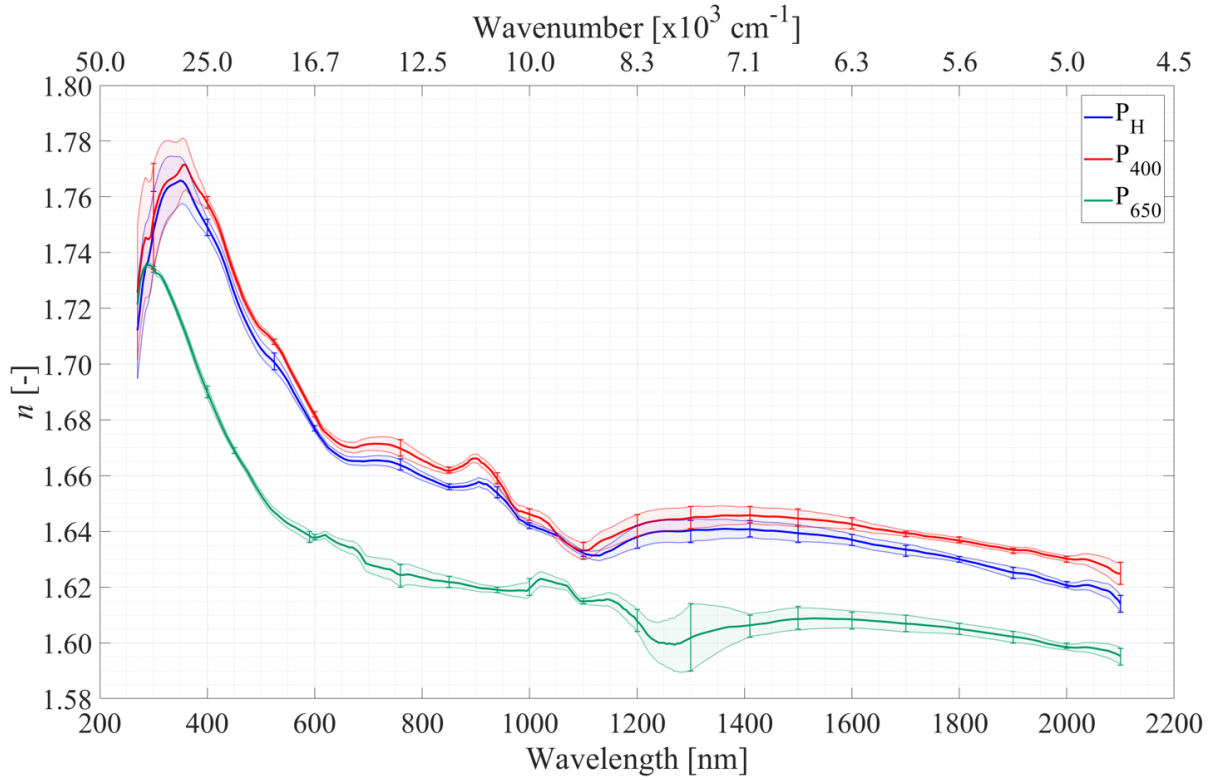
50.0   25.0   16.7   12.5   10.0   8.3   7.1   6.3   5.6   5.0   4.5

403

404   Figure 4: Real part *n* of the complex refractive index of Pluto tholins determined by spectroscopic
405   ellipsometry with a "λ-by-λ" numerical inversion method. The blue, red and green curves respectively
406   correspond to the samples P_H, P_{400} and P_{650}. The 2σ error bars were experimentally determined for
407   different wavelengths and were then linearly interpolated in-between in order to obtain the envelopes of
408   2σ uncertainty (in light blue, light red and light green). Note that the small variations observed in the *n*-
409   curves at wavelengths above 600 nm should be considered with caution.

410   In Figure 4, we observe that the values of *n* indices of P_H and P_{400} samples are relatively similar,
411   but substantially different from those of P_{650} sample. For P_H and P_{400} samples, *n*-values increase
412   from 1.71-1.73 to ~1.77 between 270 and 330 nm. Then, *n*-values decrease with a steep slope
413   from ~1.77 to around 1.67 between 330 and 650 nm. The slope attenuates between 650 and
414   1100 nm. Finally, the *n* indices of P_H and P_{400} reach an asymptotic value of 1.62-1.63 between
415   1100 and 2100 nm. For P_{650} sample, *n* index increases from 1.72 to around 1.74 between 270
416   and 305 nm, followed by a steep decrease from around 1.74 to 1.64 between 305 and 600 nm.
417   The decreasing slope then attenuates between 600 and 1200 nm, before *n* index reaches an
418   asymptotic value of 1.60-1.61 between 1200 and 2100 nm. In summary, the increase of the
419   $CH_4:N_2$ mixing ratio in the reactive gas mixture producing Pluto tholins leads to a decrease of
420   *n* index over the entire spectral range considered. As well, the maximum of *n*-value is shifted
421   towards shorter wavelengths.

422   The bell-shaped appearance between 270 and 400 nm, although not observed in the studies of

423   optical constants of Titan aerosol analogues (Brassé et al. 2015), appears to be a consistent trend

424   in Pluto tholins, whatever inversion model – "λ-by-λ" or modified Tauc-Lorentz – is used. In

425   contrast, the small variations observed in the n-curves at wavelengths above 600 nm should be

426   considered with caution. Indeed, we cannot totally rule out the fact that these small variations

427   are introduced by the n index being a function of wavelength λ (Mistrik et al. 2017; Moise et

428   al. 2015). Nevertheless, this dependence is especially observed on a large scale: when λ

429   increases, the n index increases or decreases monotonically. In addition, in the literature

430   concerning the optical constants of terrestrial aerosols or tholins materials (*e.g.,* Cechalova et

431   al. 2019; Khare et al. 1984; Liu et al. 2015; Mahjoub et al. 2012; Ramírez et al. 2002; Sciamma-

432   O'Brien et al. 2012), the n indices are often represented as a smooth profile, suggesting that

433   there may be no physical reason to observe fine-scale variations of n index.

434   The overall decreasing trend of n indices from UV to near-IR was also observed in the studies

435   of optical constants of Titan tholins, regardless of the production mode (type of energy source,

436   gas pressure, gas temperature, $CH_4:N_2$ mixing ratios…) or the type of measurement

437   (spectroscopic ellipsometry, spectrophotometry…) (Brassé et al. 2015; Imanaka et al. 2004;

438   Khare et al. 1984; Mahjoub et al. 2012, 2014; Ramírez et al. 2002; Sciamma-O'Brien et al.

439   2012; Tran et al. 2003). In the considered wavelength range, n indices of Pluto aerosol

440   analogues vary from around 1.60 to 1.78. These values are similar to the n-values determined

441   for Titan aerosol analogues (Brassé et al. 2015). It thus seems that Pluto tholins, produced in

442   gas mixtures composed of N_2, CH_4 and CO, share first-order similar optical properties with

443   Titan tholins. This similarity also extends to the chemical composition. Indeed, Jovanović et al.

444   (2020) studied the chemical composition of Pluto aerosol analogues. They showed that the

445   molecules constituting the tholins are composed of a repetition of a $(CH_2)_w(HCN)_z$ random

446   pattern, such as molecules in Titan aerosol analogues (Gautier et al. 2017; Maillard et al. 2018;

447   Pernot et al. 2010), with, however, a significant incorporation of oxygen atoms. van Krevelen

448   and te Nijenhuis (2009) reported that such n-values can also correspond to organic polymers

449   including polyamides –C(=O)–NH– and polyethers R–O–R'.

450   We also note in Figure 4 that the n indices are higher for P_H and P_{400} samples compared to the

451   P_{650} one, with a systematic difference of about 0.05 over the entire wavelength range. This

452   difference between P_H/P_{400} and P_{650} is significant and beyond the uncertainties determined for

453   the three samples at different wavelengths. Regarding the effect of $CH_4:N_2$ mixing ratio on n-

454   values, our results differ from those of Mahjoub et al. (2012). In this study concerning the

455 influence of CH$_4$ concentration on the optical constants of Titan aerosol analogues, the higher

456 the CH$_4$:N$_2$ mixing ratio, the higher the *n*-values. In the case of Pluto tholins, the relation is

457 reversed, suggesting an increasing influence of CO at lower CH$_4$ concentration.

458 Aerosols formed in Pluto's lower atmosphere (≤ 400 km of altitude) are thus expected to scatter

459 and polarize the light differently than the aerosols formed at higher altitudes (> 400 km of

460 altitude), due to their different *n* indices (Boucher 2015; Kolokolova et al. 1997; Kolokolova &

461 Jockers 1997; Nakayama et al. 2018, 2012), and therefore differently affect the photon flux

462 reaching the lower layers of the atmosphere and the surface.

463 ## 2. Effect on imaginary part *k* of the complex refractive index

464 Figure 5 shows the imaginary part *k* of the complex refractive index computed for P$_H$ (top panel,

465 blue curve), P$_{400}$ (middle panel, red curve) and P$_{650}$ (bottom panel, green curve) samples as a

466 function of wavelength. The 2σ error bars (see Table SI.4 in Supplementary Information) were

467 calculated based on the uncertainties of I_s^{exp} and I_c^{exp} for different wavelengths. The

468 uncertainties were then linearly interpolated in-between in order to obtain the envelopes of

469 uncertainty (in light blue, light red and light green).

470
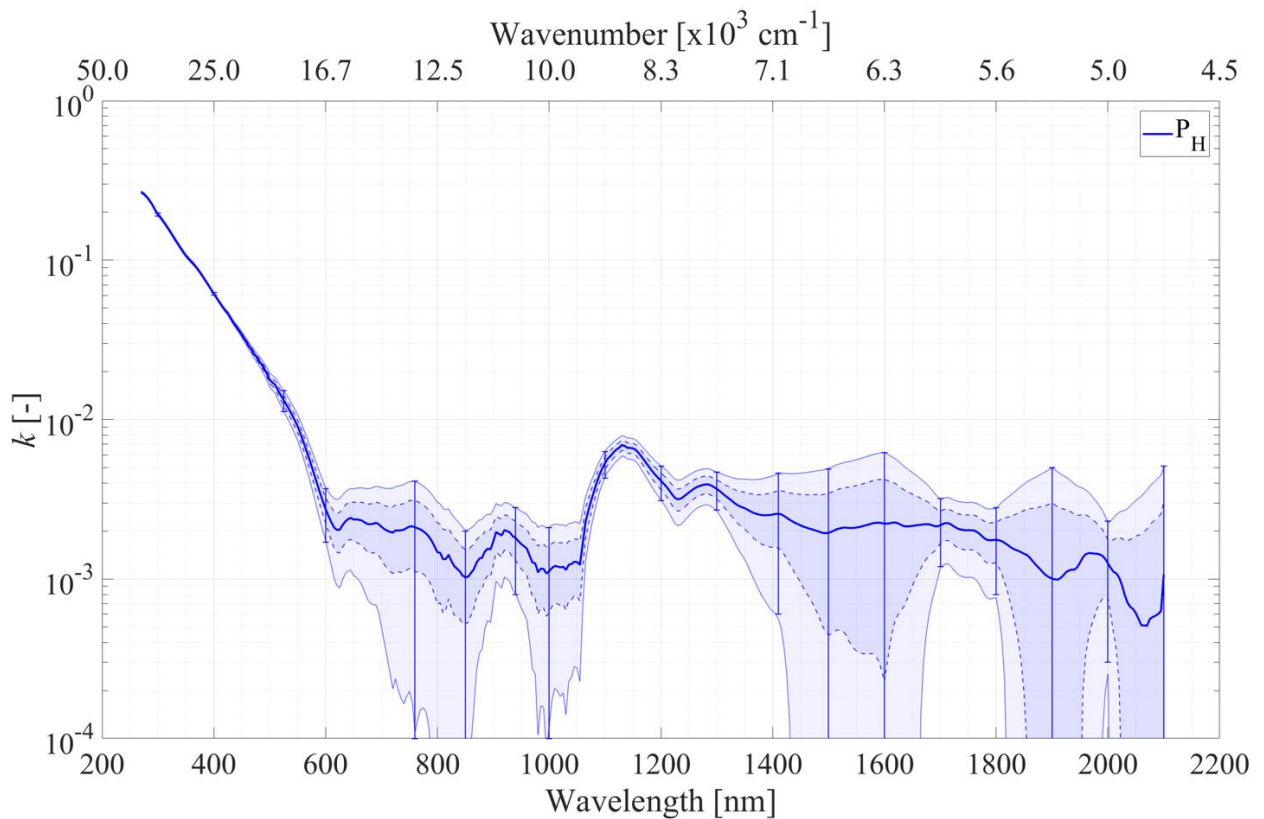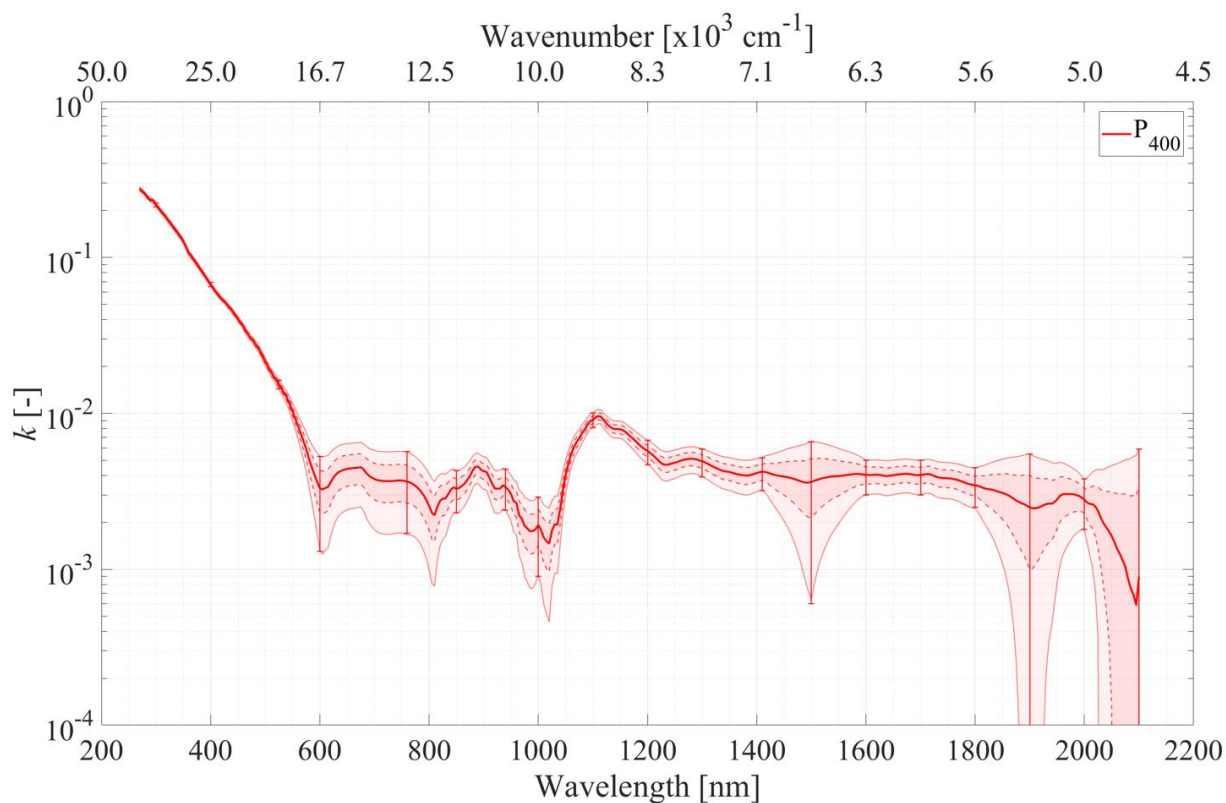
471
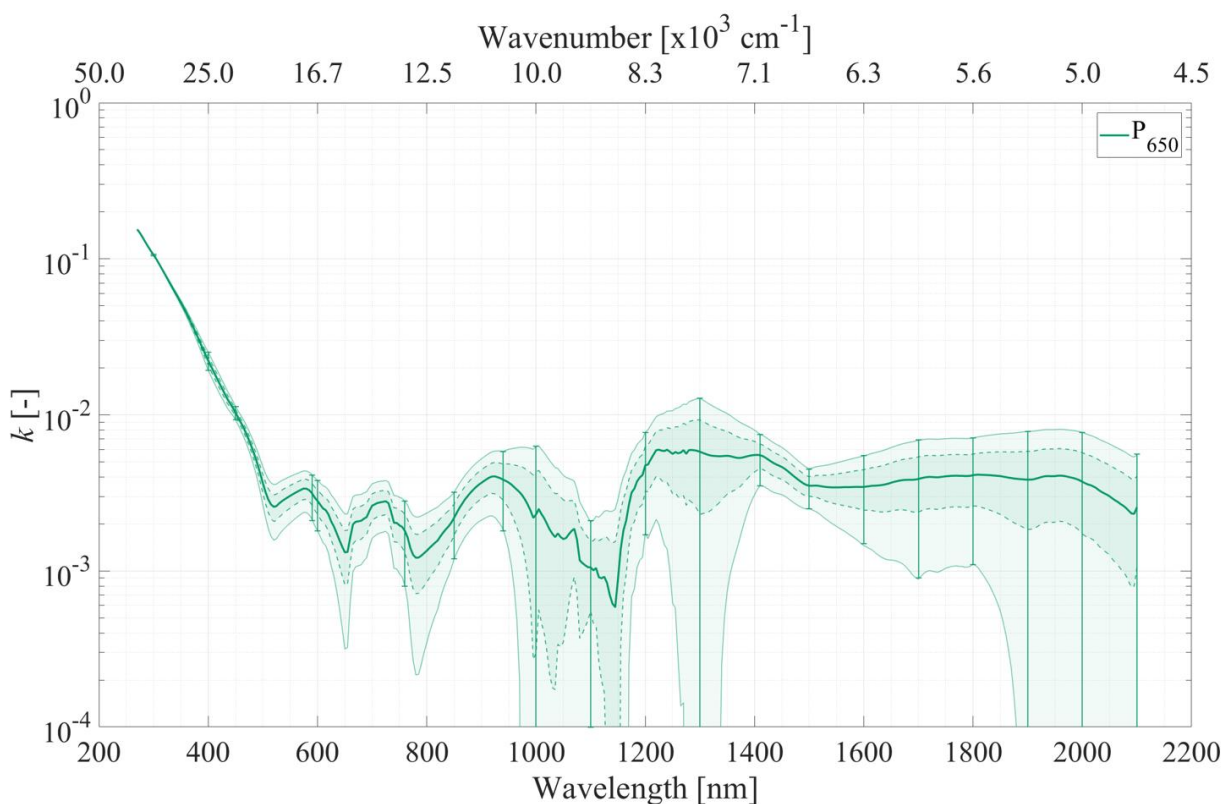
472

473   Figure 5: Imaginary part *k* of the complex refractive index of Pluto tholins determined by spectroscopic

474   ellipsometry with a "λ-by-λ" numerical inversion method. The blue (top panel), red (middle panel) and

475   green (bottom panel) curves respectively correspond to the samples P_H, P_{400} and P_{650}. The 2σ error bars

476   were experimentally determined for different wavelengths and were then linearly interpolated in-

477   between in order to obtain the envelopes of 2σ uncertainty (in light blue, light red and light green). The

478   envelopes determined by dashed lines correspond to 1σ uncertainty. The *y*-axis was cropped at 10^{-4}. The

479   2σ uncertainties of *k*-values reach 0 in the [790-850], [1450-1650] and [1820-2100] nm regions for P_H

480   sample, in the [1870-1930] and [2020-2100] nm regions for P_{400} sample and in the [980-1180], [1270-

481   1330] and [1880-2100] nm regions for P_{650} sample. Note that the large variations observed in the *k*-

482   curves at wavelengths above 600 nm should be considered with caution.

483   In Figure 5, we observe that the *k*-values of P_H and P_{400} are significantly higher for wavelengths

484   between 270 and 600 nm than those of P_{650}. From 600 to 2100 nm, the trend is less clear,

485   because of larger uncertainties on *k*-values. For P_H and P_{400} samples, *k*-values plummet from

486   2.7×10^{-1} to around 4.5×10^{-3} between 270 and 590 nm. The bandgap energy is estimated to be

487   around 590 nm. For P_{650} sample, the *k* index steeply decreases from 1.5×10^{-1} down to around

488   2×10^{-3} between 270 and 520 nm. The bandgap energy is estimated at around 520 nm. Due to

489   the large uncertainties on *k*-values determined for the three samples above 600 nm and because

490   this kind of material is weakly absorbent in the near-IR (Brassé et al. 2015), the large variations

491   observed in the *k*-curves should be considered with caution. *k* indices for all samples probably

492   reach an asymptotic value of a few 10^{-3} between 600 and 2100 nm.

493   The 2-steps behaviour of *k*-values – sharp decrease followed by a plateau – was also observed

494   for Titan aerosol analogues in the considered wavelength range (Brassé et al. 2015; Imanaka et

495   al. 2004; Khare et al. 1984; Mahjoub et al. 2012, 2014; Ramírez et al. 2002; Sciamma-O'Brien

496   et al. 2012; Tran et al. 2003).

497   We do not have a definitive explanation for the variations observed beyond 600 nm in the *k*-

498   curves of the 3 samples P_H, P_{400} and P_{650}. Nevertheless, assuming that the variations observed

499   are consistent absorption bands (see Table 2): (1) the absorption band around 725 nm observed

500   in P_{650} sample could be ascribed to C–H stretching 4th overtone in $-CH_x$ (*x* = 1, 2 and 3) and in

501   Aromatic–CH and to O–H stretching 3rd overtone in *R*–OH and in Aromatic–OH; (2) the

502   absorption band between 900 and 950 nm observed in all samples could be attributed to C–H

503   stretching 3rd overtone and to O–H stretching 2nd overtone; (3) the absorption band between

504   1100 and 1150 nm observed in P_H and P_{400} samples could correspond to C–H stretching 2nd

505   overtone and to –C=O stretching 4th overtone; (4) the absorption band between 1950 and

506   2000 nm observed in P_H and P_{400} samples could be in agreement with –C=O stretching 2nd

507   overtone in *R*–(C=O)–*R'*, *R*–(C=O)–O*R'* and in *R*–(C=O)–NH_2 and to N–H combination in *R*–

508   (C=O)–NH_2 and in aromatic amines (Stenberg et al. 2010; Workman & Weyer 2008; Xiaobo

509   et al. 2010). These overtones are conceivable, given the chemical composition determined for

510   Pluto tholins by Jovanović et al. (2020).

Wavelength [nm]	Overtone and combination near-IR band assignment	Present in sample P_x
725	• C–H stretching 4th overtone in –CH_x ($x = 1, 2$ and 3) and in Aromatic–CH • O–H stretching 3rd overtone in R–OH and in Aromatic–OH	P_{650}
900-950	• C–H stretching 3rd overtone in –CH_x ($x = 1, 2$ and 3) and in Aromatic–CH • O–H stretching 2nd overtone in R–OH and in Aromatic–OH	P_H, P_{400}, P_{650}
1100-1150	• C–H stretching 2nd overtone in –CH_x ($x = 1, 2$ and 3) and in Aromatic–CH • –C=O stretching 4th overtone in R–(C=O)–R', R–(C=O)–OR' and in R–(C=O)–NH_2	P_H, P_{400}
1950-2000	• –C=O stretching 2nd overtone in R–(C=O)–R', R–(C=O)–OR' and in R–(C=O)–NH_2 • N–H combination in R–(C=O)–NH_2 and in aromatic amines	P_H, P_{400}

514

515   From Figure 5, we can conclude that Pluto aerosol analogues significantly absorb UV and

516   visible radiations, while their absorption is more moderate above 600 nm. The strong absorption

517   below 500-600 nm, in the blue-green spectral range, agrees with a brownish colour for Pluto

518   tholins. This absorption is likely due to the presence of N- and O-bearing organic molecules

519   with lone pair, such as –NH, –NH_2, –NHR, R–N–R', –NO_2, –OH, –COOH, –C=O, R–O–R'

520   functional groups (Desyaterik et al. 2013; Imanaka et al. 2004; Liu et al. 2015; Mahjoub et al.

521   2012; Moise et al. 2015; Rao 1975). Due to the delocalization of π electrons, fused aromatic

522   rings, N- and O-containing polycyclic aromatic compounds and unsaturated molecules with

523   extensive conjugated multiple bonds also participate to the strong absorption of UV and visible

524 wavelengths (D'Amico et al. 1980; Desyaterik et al. 2013; Imanaka et al. 2004; Lambe et al.

525 2013; Liu et al. 2015; Moise et al. 2015; Rao 1975; Tran et al. 2003; Zhong et al. 2012). Most

526 of these chemical functions were actually detected in Pluto aerosol analogues by Jovanović et

527 al. (2020), who showed the presence of unsaturated N- and O-bearing molecules in large

528 amount.

529 When CH_4 concentration increases, the bandgap energy shifts towards shorter wavelengths.

530 k index thus depends on the CH_4:N_2 mixing ratio used to produce the tholins. Indeed, from 270

531 to around 600 nm, where the uncertainties are low, we can see that P_H and P_{400} samples,

532 produced with a lower CH_4 concentration, present higher k-values than P_{650} sample, produced

533 with a higher CH_4 concentration.

534 This anti-correlation between k-values and CH_4:N_2 mixing ratio was also detected by Mahjoub

535 et al. (2012) in their study concerning Titan tholins. They attributed this anti-correlation to the

536 proportion of N-bearing molecules: when CH_4 concentration decreases, N-containing

537 molecules increase in proportion and contribute to a higher absorption of UV and visible

538 radiations (Mahjoub et al. 2012, 2014). This conclusion was also proposed by Imanaka et al.

539 (2004), when comparing their Titan tholins with Uranus/Neptune tholins from Khare et al.

540 (1987) study, produced in CH_4:H_2 gas mixtures. They hypothesized that N-incorporation in

541 Titan tholins could increase k-values in the UV-Vis spectral range, in agreement with the

542 laboratory experiments realized by Scattergood and Owen (1977). Indeed, nitrogen promotes

543 unsaturation. When N_2 content is increased in the reactive gas mixture forming Pluto tholins

544 (case of P_H and P_{400} samples), the formation of sp^2 bonds is favoured. In contrast, when the

545 reactive gas mixture contains more CH_4 (case of P_{650} sample), the presence of large amounts of

546 hydrogen promotes the formation of sp^3 bonds, which have no effect on π-π* electronic

547 transitions in UV and visible wavelength ranges (Ferrari et al. 2003; Quirico et al. 2008).

548 Another explanation to both higher n- and k-values for P_H and P_{400} could be the higher oxidation

549 of these samples. Indeed, Jovanović et al. (2020) showed that P_{400} sample contains more oxygen

550 in mass than P_{650}. Studies realized on optical properties of terrestrial secondary organic aerosols

551 (Cappa et al. 2011; Lambe et al. 2013; Moise et al. 2015; Nakayama et al. 2018, 2012) and of

552 oxidized Early Earth- and Exoplanets-like aerosols (Gavilan et al. 2017) showed that n indices

553 increase when the oxidation level of the aerosols increases. Moreover, the more the aerosols

554 are oxidized, the more they absorb UV and visible radiations.

555 We can thus expect that aerosols formed at different altitudes in Pluto's atmosphere will
556 differently absorb radiations reaching the atmosphere. In particular, Pluto's aerosols formed at
557 or below 400 km of altitude above the surface, due to their higher N- and O-content, may absorb
558 more UV and visible wavelengths than aerosols formed above 400 km of altitude.

559 Besides, as mentioned in Section II.1, the samples studied here could also be considered as
560 analogues of aerosols produced during different seasons or epochs of Pluto (Bertrand et al.
561 2019; Bertrand & Forget 2016; Stern et al. 2017a). In Bertrand and Forget (2016), their Pluto
562 General Circulation Model (GCM) predicted a mean CH_4 atmospheric mixing ratio in ~2200
563 (terrestrial year; northern winter/southern summer on Pluto) ~5 times higher than that observed
564 in 2015. This is due to the condensation of N_2 onto the surface, which also leads to a decrease
565 in surface pressure as low as 10^{-5}-10^{-6} mbar; the atmosphere being thinner, the methane is less
566 diluted (Bertrand & Forget 2016; Stern et al. 2017a). However, considering that the pressure in
567 the atmosphere would still be sufficient to allow the formation of haze particles (Johnson et al.
568 2021), one would expect less absorbent aerosols, such as P_{650} tholins, differently affecting the
569 thermal profile of Pluto and the photon flux reaching the surface.

570 **V.   New input parameters for Pluto atmospheric and surface models**

571 In this section, we first compare the optical constants determined in this study with those from
572 the study by Khare et al. (1984). Then, we discuss the application of our Pluto tholins optical
573 constants to the modelling of Pluto's surface and atmosphere.

574 **1. Comparison of our optical constants with those of Titan tholins from the study by**
575 **Khare et al. (1984)**

576 Khare et al. (1984) did a pioneer work to determine the optical constants *n* and *k* of Titan aerosol
577 analogues from soft X-ray to microwave frequencies. For this purpose, they combined
578 transmittance, specular reflectance, interferometric, Brewster angle and ellipsometric
579 polarization measurements on thin films synthesized on various substrates. Although the large
580 considered wavelength range is valuable, the employed method – combination of different thin
581 films and different measurement techniques, with interpolations – induces major uncertainties.
582 Moreover, Brassé et al. (2015) reviewed why Khare et al. (1984) optical constants are not
583 representative of Titan's aerosols at different wavelengths.

584 Even though several other teams have since then determined optical properties of Titan aerosol
585 analogues (Imanaka et al. 2012; Mahjoub et al. 2012, 2014; Ramírez et al. 2002; Sciamma-

586   O'Brien et al. 2012; Tran et al. 2003; Vuitton et al. 2009), optical constants from Khare et al.

587   (1984) are still widely used by the modelling teams to explain atmospheric and surface

588   properties of Titan, often by introducing *ad hoc* modifications to them to fit the observations

589   better (Brossier et al. 2018; Fan et al. 2019; Griffith et al. 2012; Lavvas et al. 2009; Liang et al.

590   2007; Lopes et al. 2016; Seignovert et al. 2017), but also of Pluto (Cheng et al. 2017; Grundy

591   et al. 2018; Protopapa et al. 2017, 2020; Young et al. 2018; Zhang et al. 2017). This is partially

592   due to the lack of optical constants of tholins-like materials covering a wide wavelength range.

593   Only the data by Khare et al. (1984) and Tran et al. (2003) for Titan tholins cover the same

594   wavelength range as the Pluto optical constants determined in this work, and therefore are used

595   for comparison purposes. In Figures 6 and 7, we respectively compare the *n* index and the *k*

596   index of Pluto aerosol analogues P_{400} (red asterisks) to Khare et al. (1984) data (black asterisks),

597   from 270 to 2100 nm. Note that Titan tholins from Khare et al. (1984) were produced in a

598   reactive gas mixture composed of 90% of N_2 and 10% of CH_4.
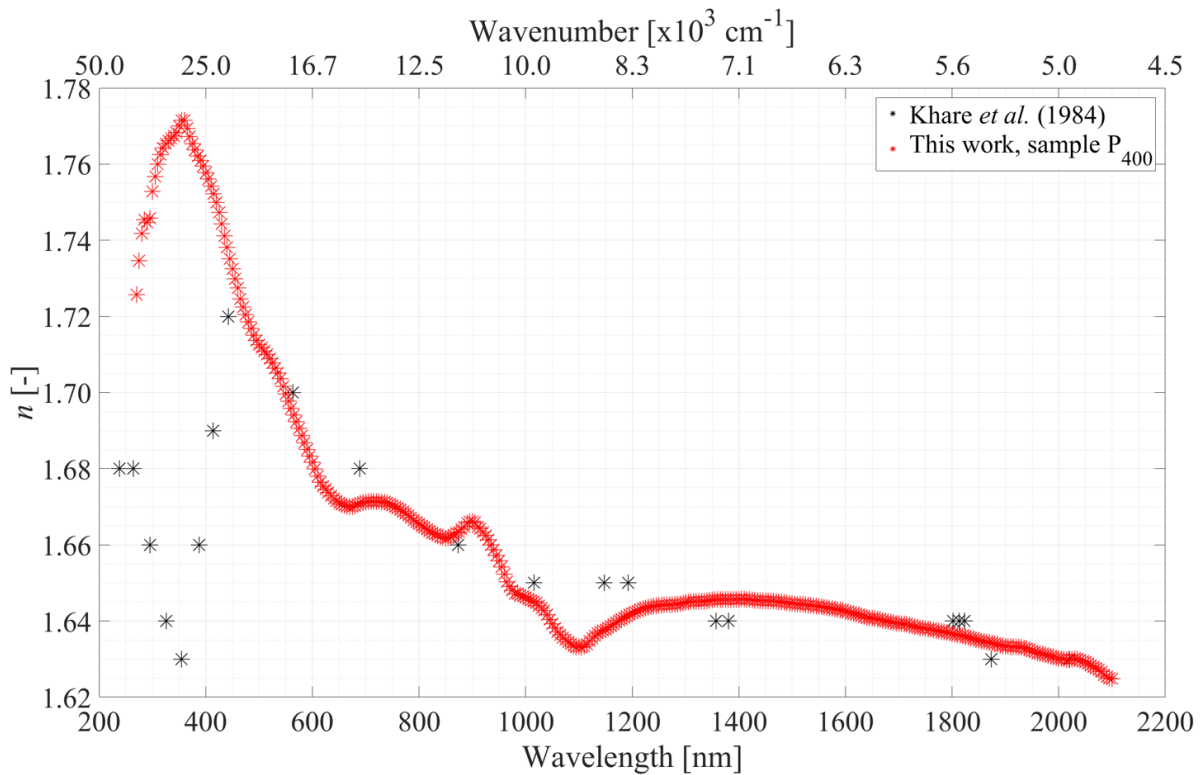

599

600   Figure 6: Comparison between the real part *n* of the complex refractive index of our Pluto tholins P_{400}

601   (red asterisks) and Titan tholins from Khare et al. (1984) study (black asterisks).
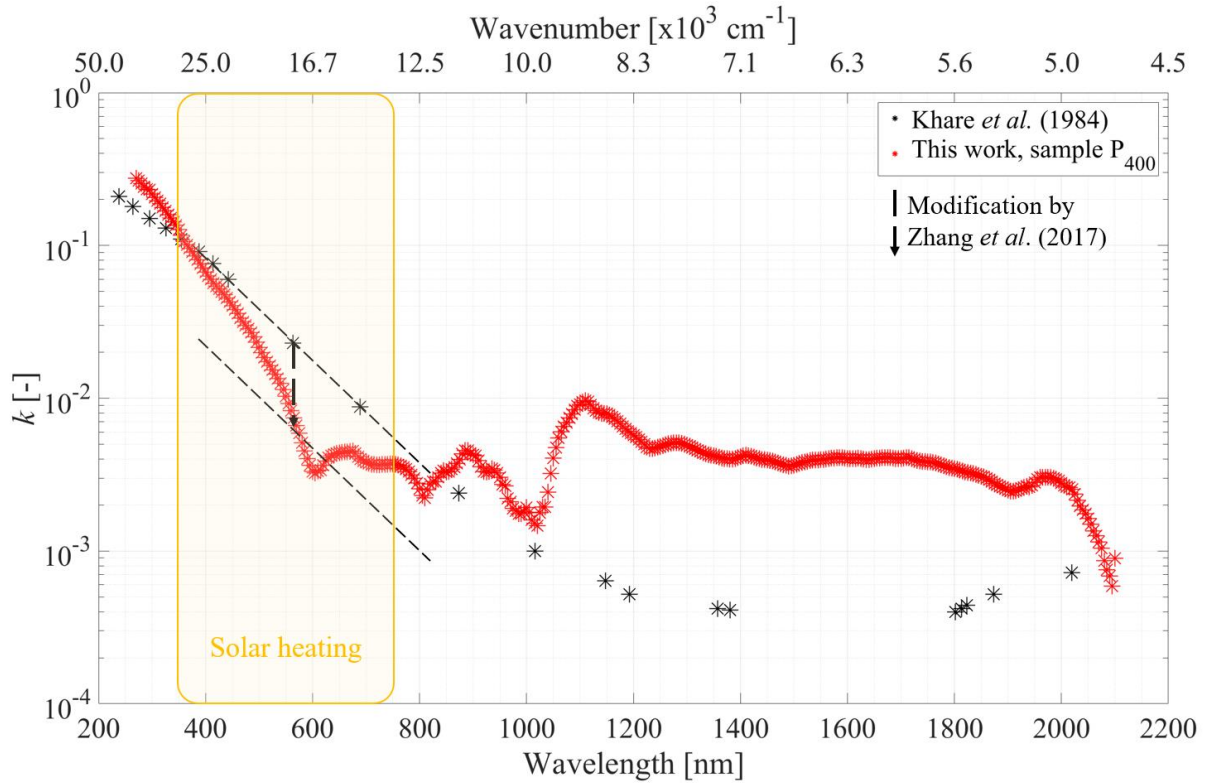
602

Figure 7: Comparison between the imaginary part k the complex refractive index of our Pluto tholins
P_{400} (red asterisks) and Titan tholins from Khare et al. (1984) study (black asterisks). The black dashed
arrow indicates the modification implemented by Zhang et al. (2017) to the k-values from Khare et al.
(1984) in the region where solar heating dominates (represented by the yellow rectangle) in order to
adjust Pluto's thermal balance.

In Figure 6, we observe that the n index of Pluto tholins P_{400} is similar to that of Khare et al.
(1984) Titan tholins from 450 to 2100 nm. Below 450 nm, the behaviour is reversed. While n-
value reaches a maximum near 330 nm for P_{400}, Khare et al. (1984) data present a minimum n-
value near 350 nm. We do not have a definitive explanation for this behaviour of Khare et al.
(1984) n index, but it could be due to a low sampling combined with interpolation, a poor
definition of the optical properties of the substrates used for the synthesis of the tholins thin
films, or the light source used for the measurements being at the limit of its range.

Concerning the k indices (Figure 7), the bandgap energy of Khare et al. (1984) tholins is shifted
towards longer wavelengths (around 1200 nm) compared to P_{400} sample (around 590 nm). k-
values of P_{400} are higher than those of Khare et al. (1984) below 380 nm and in the near-IR
(> 900 nm). These higher values can be explained by higher N- and O-content of Pluto aerosol
analogues P_{400} (Cappa et al. 2011; Gavilan et al. 2017; Imanaka et al. 2004; Jovanović et al.
2020; Lambe et al. 2013; Mahjoub et al. 2012; Nakayama et al. 2018, 2012; Quirico et al. 2008).

621 From 380 to around 800 nm, k-values of P_{400} are lower than those of Khare et al. (1984), due

622 to the shifted bandgap energy which is caused by higher k-values in the UV and a steeper slope

623 in the UV-Vis for our P_{400} sample.

624 Even though k-values of P_{400} sample are one order of magnitude higher than those of Khare et

625 al. (1984) between 1000 and 2000 nm, they are constant and do not present the anomalous sharp

626 increase beyond 1800 nm presented by the Khare et al. (1984) k-values. The fact that our k-

627 values are one order of magnitude higher in the near-IR is consistent with published literature

628 on Titan's aerosols. For example, Lavvas et al. (2010) and Larson et al. (2015) reported that the

629 actual optical properties of Titan's aerosols should be about an order of magnitude larger in the

630 near-IR compared to the optical constants from Khare et al. (1984).

631 **2. Application of our optical constants to Pluto's surface modelling**

632 Recently, Protopapa et al. (2020) studied the colouring materials across Pluto's surface. To

633 support the conclusion developed by Grundy et al. (2018), Pluto's photochemical aerosols were

634 considered as potential surface colouring agent. Thus, in their model, they implemented the

635 k indices determined for Titan tholins by Khare et al. (1984) and Tran et al. (2003).

636 Nevertheless, in order to fit their models to spectra acquired in the regions of Cthulhu Macula

637 and Lowell Regio by the imagers MVIC (Multispectral Visible Imaging Camera, a Vis-near-IR

638 [400-975 nm] imager) and LEISA (Linear Etalon Imaging Spectral Array, an IR [1.25-2.5 µm]

639 spectral imager) constituting the Ralph instrument (Reuter et al. 2008), some modifications of

640 k indices by Khare et al. (1984) were necessary. Specifically, Protopapa et al. (2020): first

641 applied no change to the n index of Khare et al. (1984); secondly decreased the k-value of Khare

642 et al. (1984) at 690 nm by ~55% to match the observations of Pluto in the *RED* filter between

643 540 and 700 nm (note that Protopapa et al. (2020) preserved the original sampling of Khare et

644 al. (1984) explaining why the k-value was modified at 690 nm); and thirdly assumed k index to

645 be constant between 1800 and 2200 nm, given that the increase displayed by the k-values of

646 Khare et al. (1984) beyond 1.8 µm was not consistent with the observations.

647 Figure 8 was adapted from Protopapa et al. (2020). It displays the imaginary part k of the

648 complex refractive index (right y-axis) of our P_{400} sample (red curve, with an envelope of

649 uncertainties represented in salmon pink), compared to those of the Titan tholins from the

650 studies by Khare et al. (1984) (orange triangles) and Tran et al. (2003) (blue dots). Additionally,

651 the set of k indices determined by Protopapa et al. (2020) (black squares) that best fits the MVIC

652 and LEISA *New Horizons* measurements acquired in the regions of Cthulhu Macula and Lowell

653 Regio are shown, as well as the MVIC transmission filters (left *y*-axis). The reader is referred

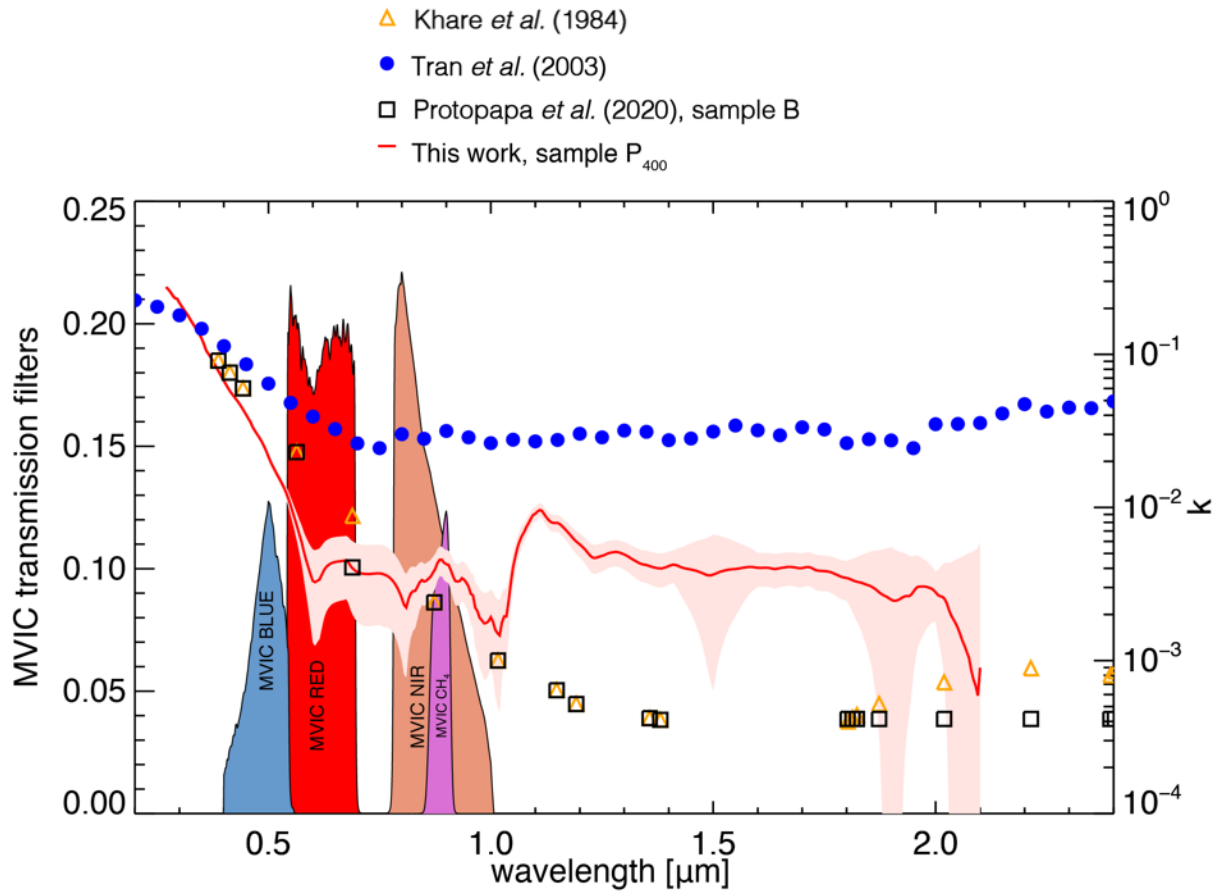654 to Protopapa et al. (2020) for details about the modelling of MVIC and LEISA spectra.

Figure 8: Figure adapted from Protopapa et al. (2020). Imaginary part *k* of the complex refractive index (right *y*-axis) is represented as a function of wavelength. The red curve with the salmon-pink envelope corresponds to the *k* index of our sample P_{400}. The orange triangles correspond to the *k* index determined by Khare et al. (1984), while the blue dots are from the study by Tran et al. (2003). The black squares are the *k*-values determined by Protopapa et al. (2020) that best fit the MVIC and LEISA data. The MVIC transmission filters (left *y*-axis) are shown for reference. The reader is referred to Protopapa et al. (2020) for details about the modelling.

663 Protopapa et al. (2020) recognized that the *k*-values of Titan tholins by Khare et al. (1984)

664 present a sharp increase beyond 1.8 µm (Figure 8, orange triangles), inconsistent with the Pluto

665 *New Horizons* data. Therefore, Protopapa et al. (2020) modified the *k*-values by Khare et al.

666 (1984) beyond 1.8 µm assuming them to be constant with wavelengths up to 2.4 µm and equal

667 to the mean value computed between 1.35 and 1.45 µm (see Figure 8, sample B from Protopapa

668 et al. (2020)). This is consistent with our direct values for Pluto tholins P_{400}. Indeed, as noted

669 above, while the *k*-values of P_{400} sample are one order of magnitude higher than those of Khare

670   et al. (1984) between 1000 and 2000 nm, they are constant with wavelengths and do not display

671   the sharp increase beyond 1.8 µm presented by the Khare et al. (1984) *k*-values.

672   In Figure 8, we observe that the change to the Khare et al. (1984) data implemented at 690 nm

673   by Protopapa et al. (2020) (black squares) to match the Pluto *New Horizons* observations is

674   consistent with the *k*-curve of our Pluto tholins P_{400} (red curve, with the salmon-pink envelope).

675   Also, sample B from Protopapa et al. (2020) shares the same slope in the UV-Vis as our P_{400}

676   sample and is in agreement, within the uncertainties, with our data between 0.8 and 1.0 µm.

677   These considerations support the suitability of our optical constants to reproduce Pluto

678   compositional observations at least in the UV and visible spectral ranges. Nevertheless, from

679   1.1 to 1.8 µm, our *k*-values are obviously larger by an order of magnitude with respect to the *k*-

680   values adopted to reproduce Pluto *New Horizons* data by Protopapa et al. (2020). An in-depth

681   modelling analysis of the Pluto *New Horizons* observations using as inputs our Pluto tholins

682   optical constants throughout the full wavelength range, from 0.4 to 2.5 µm, is required to

683   confirm that Pluto's colouration and composition can be attributed to the photochemical

684   aerosols that we reproduced in our laboratory.

685   **3. Application of our optical constants to Pluto's atmosphere modelling**

686   In order to evaluate the effect of our Pluto tholins optical constants on aerosol properties, and

687   to compare with those of Titan, we display the extinction coefficient Q_{ext} (Figure 9), the single-

688   scattering albedo ω (Figure 10), and the absorption coefficient Q_{abs} (Figure 11) for a spherical

689   particle of 10 nm according to Mie theory (formalized in Bohren & Huffman (1983)) and for a

690   fractal aggregate of spheres (Rannou et al. 1997, 1999).

691   These parameters are key in the atmospheric radiative transfer (Bohren & Huffman 1983). Q_{ext}

692   is the ratio of the extinction cross section (σ_{ext}) and the geometric projection of the particle

693   (σ_{geo}). It characterizes the extinction, *i.e.* the absorption and scattering of radiation by aerosols.

694   ω represents the fraction of scattered radiation, while $(1 - \omega)$ represents the fraction of absorbed

695   radiation. ω is equal to 0 for a perfect absorber and equal to 1 for a perfect scatterer. These two

696   coefficients control the amount of energy absorption by aerosols at solar wavelengths through

697    $Q_{abs} = (1 - \omega) \times Q_{ext}$ and the emission in thermal infrared $Q_{emi} = Q_{abs} = (1 - \omega) \times Q_{ext}$.

698   They participate to the thermal balance of Pluto's atmosphere, as demonstrated by Zhang et al.

699   (2017).

700   At first glance, the scattering of haze at Pluto's limb in the forward direction indicates particles

701   having radii in the range 0.1-0.5 µm (Gladstone et al. 2016; Stern et al. 2015). Further detailed

702   analyses and arguments from microphysical models (Cheng et al. 2017; Gao et al. 2017; Zhang

703   et al. 2017) yielded a better result with fractal aggregates of small grains. In these studies, a

704   fractal dimension $D_f = 2$ was assumed, the morphology of the haze particles is thus more like

705   that of snowflakes instead of solid spheres. The study by Cheng et al. (2017) showed that

706   spherical monomers should have ~10 nm radius (R_m) and aggregates should have a "bulk

707   radius" (or "volume equivalent radius") of about $R_b = 0.15$ µm, corresponding to

708     $\mathcal{N} = (R_b/R_m)^3 \approx 3375$ monomers per aggregate. Such a fractal structure globally satisfies,

709   although not perfectly, the main requirements to explain Pluto *New Horizons* observations

710   (Cheng et al. 2017). This aerosol structure was also used by Zhang et al. (2017) to study Pluto's

711   thermal balance. Note, however, that in the study by Gao et al. (2017), the particle size

712   distributions of their model are displayed as a function of the "effective radius" R_f. Since their

713   aerosols grow up to $R_f = 0.15$ µm, with a fractal dimension $D_f = 2$, the corresponding aggregates

714   appear much smaller ($\mathcal{N} = 225$) than those considered by Cheng et al. (2017), Zhang et al.

715   (2017) and Lavvas et al. (2020) ($\mathcal{N} = 3375$). The most probable reason for this difference stands

716   in that Cheng et al. (2017) and Lavvas et al. (2020) matched data from *New Horizons* containing

717   information about the aerosol size, with observations made at different phase angles, while Gao

718   et al. (2017) used data that are not sensitive to the aerosol size. Since aerosols are produced

719   from growth mechanisms, they are expected to start as small spherical particles at high altitudes

720   and continuously get larger by coagulation (direct gas-particle interactions) while sedimenting

721   (Cheng et al. 2017; Gao et al. 2017; Zhang et al. 2017). Thus, both the properties of small

722   spherical monomers and fractal aggregates are interesting.

723   In Figures 9 and 10, we compare, for several sets of optical constants, the parameters Q_{ext} and

724   ω computed for spherical monomers of 10 nm radius, distributed with a log-normal distribution

725   and an effective variance ν of 0.03 (dotted lines), and for fractal aggregates of 3375 monomers

726   of 10 nm radius (plain lines). We used the optical constants determined in this work (P_H, P_{400}

727   and P_{650}, in blue, red and green respectively), optical constants determined for Titan tholins by

728   Khare et al. (1984) (in black) and for Titan's aerosols from observations by Rannou et al. (2010)

729   and Vinatier et al. (2012) (in pink).

Spheres of 10 nm (ν = 0.03) Mie model (Bohren & Huffman, 1983)	Fractal aggregates of 3375 spheres of 10 nm Rannou *et al.* (1997, 1999)
····· Khare *et al.* (1984) / Zhang *et al.* (2017)	—— Khare *et al.* (1984) / Zhang *et al.* (2017)
····· Rannou *et al.* (2010) + Vinatier *et al.* (2012)	—— Rannou *et al.* (2010) + Vinatier *et al.* (2012)
····· This work, sample P_H	—— This work, sample P_H
····· This work, sample P_{400}	—— This work, sample P_{400}
····· This work, sample P_{650}	—— This work, sample P_{650}

730
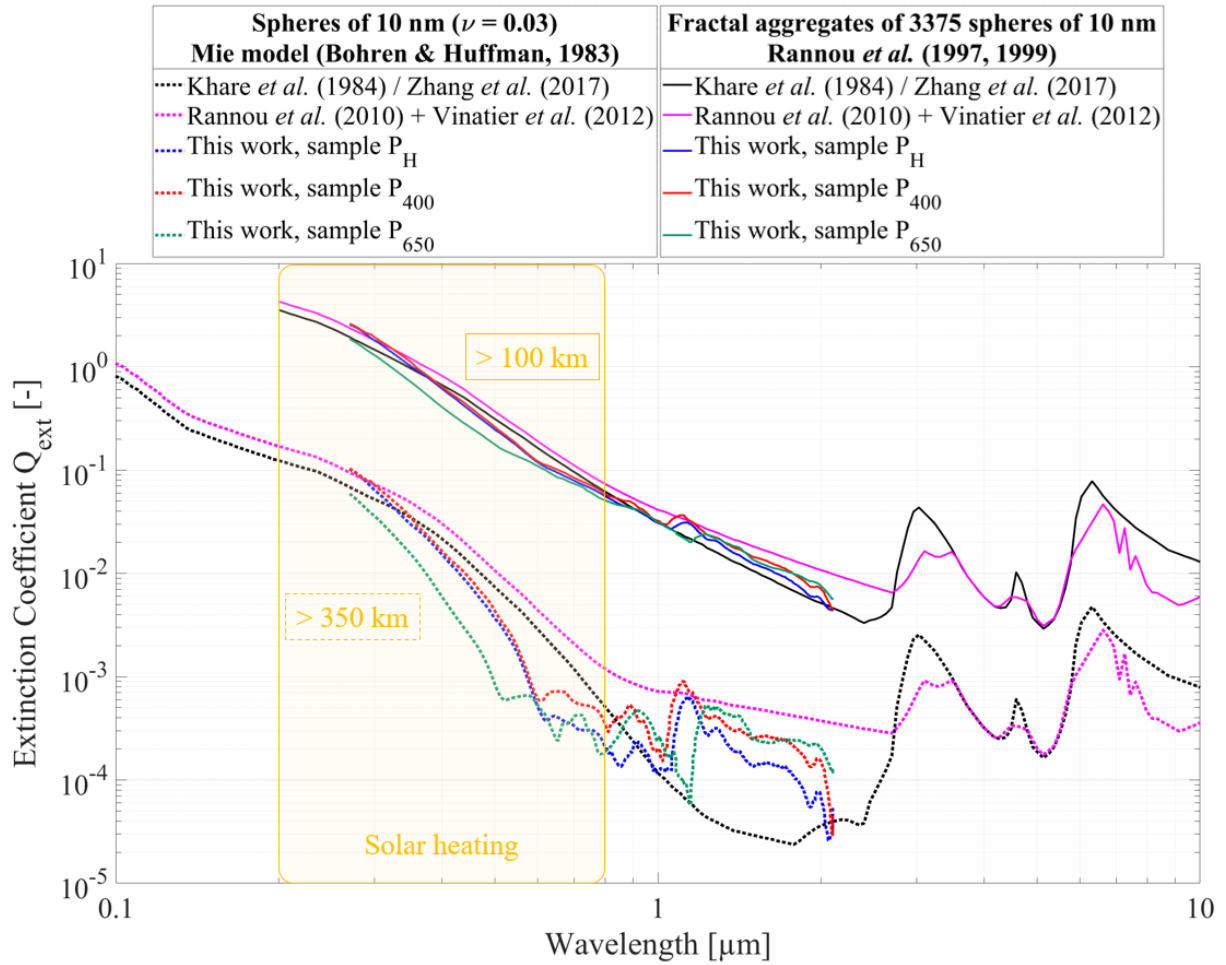
Figure 9: Extinction coefficients Q_{ext} determined for spherical monomers of 10 nm radius (log-normal distribution, with effective variance ν = 0.03) with a Mie model formalized in Bohren & Huffman (1983) (dotted curves) and for fractal aggregates of 3375 monomers of 10 nm radius with the model developed by Rannou et al. (1997, 1999) (plain curves). The black curves were generated with the optical constants determined by Khare et al. (1984) for Titan tholins. Note that these Khare et al. (1984) optical constants were adopted in Zhang et al. (2017) study. The pink curves were generated with the optical constants determined by Rannou et al. (2010) and Vinatier et al. (2012) for Titan's aerosols. The blue, red and green curves were generated with the optical constants determined respectively for our samples P_H, P_{400} and P_{650}. The yellow rectangle indicates the region where solar heating dominates. The dotted curves (spherical monomers) give information on the radiative transfer in the upper layers of Pluto's atmosphere (> 350 km of altitude), while the plain curves (fractal aggregates) give information on the radiative transfer in Pluto's lower atmosphere (between 100 and 300 km of altitude).
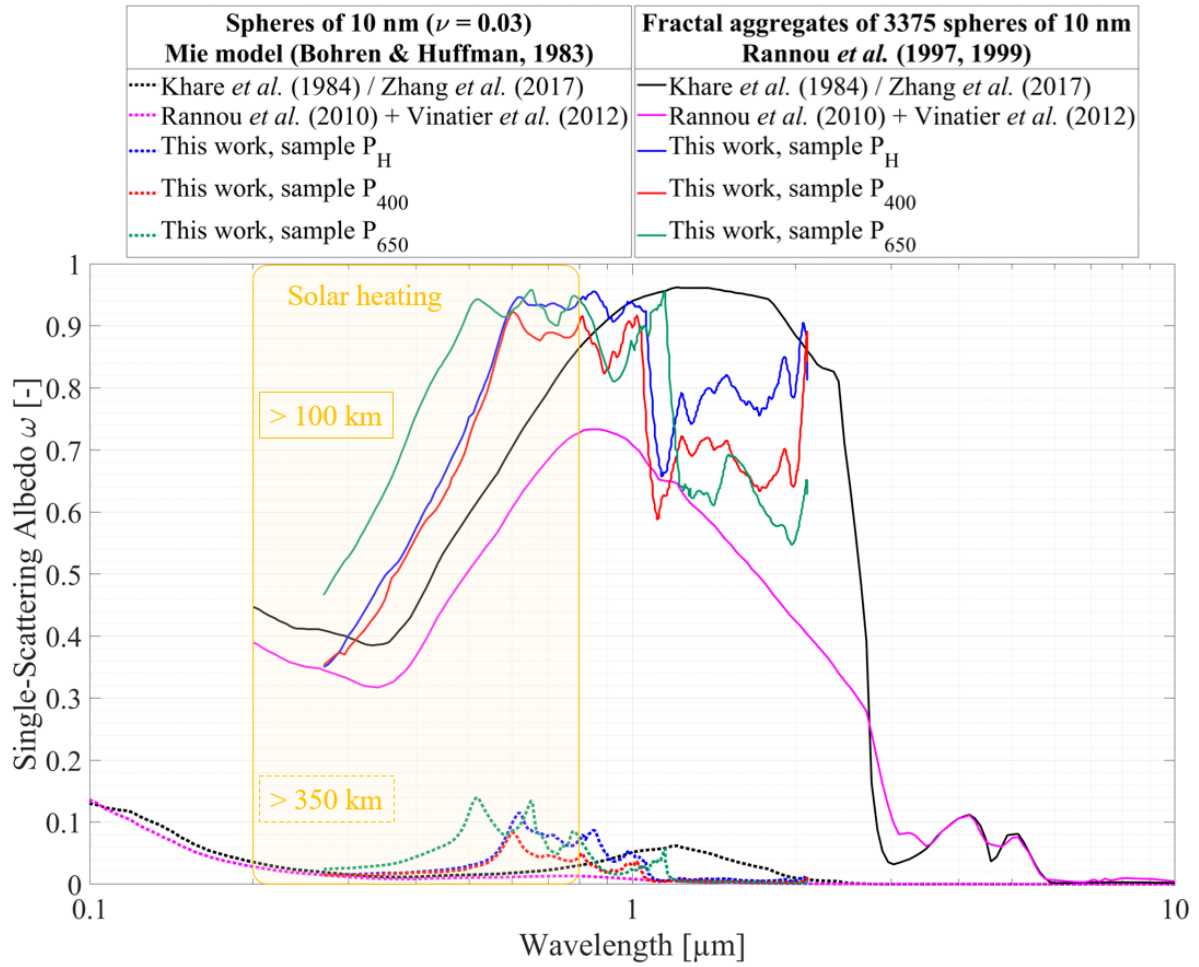
Spheres of 10 nm ($\nu = 0.03$) Mie model (Bohren & Huffman, 1983)	Fractal aggregates of 3375 spheres of 10 nm Rannou *et al.* (1997, 1999)
···· Khare *et al.* (1984) / Zhang *et al.* (2017)	— Khare *et al.* (1984) / Zhang *et al.* (2017)
···· Rannou *et al.* (2010) + Vinatier *et al.* (2012)	— Rannou *et al.* (2010) + Vinatier *et al.* (2012)
···· This work, sample P_H	— This work, sample P_H
···· This work, sample P_{400}	— This work, sample P_{400}
···· This work, sample P_{650}	— This work, sample P_{650}

Figure 10: Same as Figure 9, but showing the single-scattering albedo ω.

In Figure 9, we remark that the extinction coefficients Q_{ext} for spherical particles or fractal aggregates computed with tholins relevant for Pluto have a steepest spectral slope at visible wavelengths (broadly from 0.2 to 0.8 µm, where most Pluto *New Horizons* photometrical data were taken, and where solar heating occurs) than those computed with optical constants relevant for Titan's aerosols.

In Figure 10, considering single spheres or fractal aggregates, we see that the single-scattering albedo ω is significantly higher in the UV and visible spectral ranges with the optical constants of Pluto tholins than with Titan optical constants. In the near-IR, ω of Pluto tholins are lower than that of Khare et al. (1984) Titan tholins. This suggests that Pluto's haze absorbs less in the UV-Vis wavelength range than Titan's haze.

However, to really assess the absorption efficiency of each type of particles, one has to compare the absorption coefficients $Q_{abs} = (1 - \omega) \times Q_{ext}$ (displayed in Figure 11).

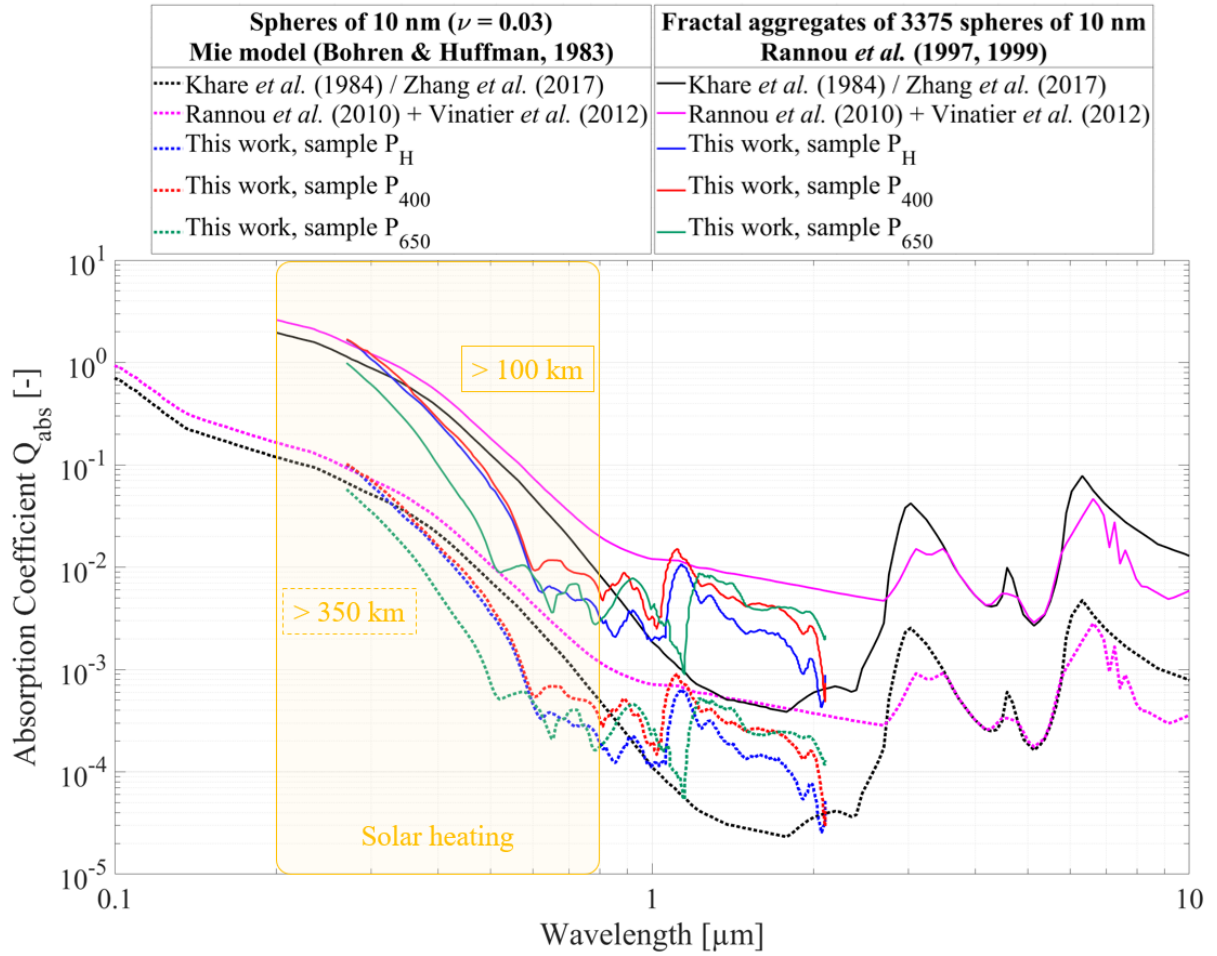| Spheres of 10 nm ($\nu = 0.03$) Mie model (Bohren & Huffman, 1983)	Fractal aggregates of 3375 spheres of 10 nm Rannou *et al.* (1997, 1999)
⋯⋯ Khare *et al.* (1984) / Zhang *et al.* (2017)	—— Khare *et al.* (1984) / Zhang *et al.* (2017)
⋯⋯ Rannou *et al.* (2010) + Vinatier *et al.* (2012)	—— Rannou *et al.* (2010) + Vinatier *et al.* (2012)
⋯⋯ This work, sample P_H	—— This work, sample P_H
⋯⋯ This work, sample P_{400}	—— This work, sample P_{400}
⋯⋯ This work, sample P_{650}	—— This work, sample P_{650}

757

Figure 11: Same as Figure 9, but showing the absorption coefficients Q_{abs}.

759   The absorption coefficients Q_{abs} (Figure 11) computed with Pluto tholins optical constants are

760   about equal to those computed with Titan optical constants at 0.3 µm. Nevertheless, they drop

761   much faster with wavelengths and are lower by a factor 3 to 10 at wavelengths larger than ~0.4-

762   0.5 µm. This is true for small spherical particles and fractal aggregates.

763   Beyond 1 µm, the marked structures of Pluto tholins set the extinction coefficients Q_{ext} (Figure

764   9) between those obtained with optical constants of Khare et al. (1984) and Rannou et al. (2010),

765   but this has less consequence on data analysis or on the thermal balance. On the other hand, the

766   scattering efficiency $Q_{sca} = \omega \times Q_{ext}$, the phase functions and the asymmetry parameters are

767   not modified at all by optical constants (see Supplementary Information, Figures A and B).

768   This has an important consequence: using other optical constants than those already used to

769   analyse scattering photometry at Pluto's limb (Cheng et al. 2017; Gao et al. 2017; Gladstone et

770   al. 2016; Stern et al. 2015) would not change the result about aerosol size and vertical profile.

771   Nevertheless, optical constants of Pluto tholins presented in this study deeply modify the link

772 between the scattering properties and the absorption properties, compared to Titan tholins. That

773 is, for the same scattering efficiency, Pluto tholins absorb about 5 to 10 times less than Titan

774 tholins at 0.5 µm (effective wavelength of solar input).

775 To adjust Pluto's thermal balance, Zhang et al. (2017) used the optical constants from Khare et

776 al. (1984), and had to decrease significantly (up to a factor 4) the absorption efficiency of

777 aerosols in the visible wavelength range (see Figure 7, black dashed arrow), to increase it in

778 thermal IR and grossly keep the same extinction properties to match Alice UV spectrometer

779 retrieval for the haze extinction (Stern et al. 2015). Here we see that low absorption is a natural

780 outcome of Pluto tholins produced for this study with chemical conditions representative of

781 Pluto's atmosphere.

782 **VI.   Conclusion and Perspectives**

783 In this study, we determined the optical constants of Pluto aerosol analogues. Three types of

784 tholins were produced from gas mixtures with different $N_2:CH_4:CO$ proportions, in order to

785 mimic aerosols formed at different altitudes in Pluto's current atmosphere. The sample P_H is

786 expected to be representative of aerosols formed below 350 km of altitude above the surface.

787 The sample P_{400} is expected to mimic the aerosols formed at around 400 km of altitude. The

788 sample P_{650} is expected to be analogous of aerosols formed between 600 and 700 km of altitude.

789 These three gas mixtures differing in their $CH_4:N_2$ mixing ratio can also be considered as

790 analogues of Pluto's atmosphere at different seasons or epochs.

791 Our results show:

792   (1) A strong absorption of UV and visible radiations by Pluto tholins, attributed to their N-
793   bearing and O-bearing organic molecules.
794   (2) A moderate absorption in the near-IR spectral range by Pluto tholins with k indices of a
795   few 10^{-3}.
796   (3) A dependency of n and k indices to the $CH_4:N_2$ mixing ratio, and thus to the altitude of
797   aerosol formation in Pluto's atmosphere. The N- and O-content in Pluto low-altitude
798   aerosols is enhanced, leading to an increase of both n- and k-values. This dependency
799   of the optical constants to the $CH_4:N_2$ mixing ratio has also implications for the seasonal
800   and past epochal radiative transfer of Pluto.

801 The comparison of our data with the optical constants determined for Titan tholins by Khare et

802 al. (1984) shows that Pluto tholins present globally similar n-values to those of Titan. However,

803 differences are observed concerning the k indices. In particular, k-values of Pluto tholins are

804 one order of magnitude higher than those of Titan in the near-IR. In the UV spectral range,

805 k indices of Pluto tholins are also higher, which is probably due to the reactivity of nitrogen and

806 carbon monoxide in the gas mixture producing Pluto's aerosols.

807 The optical properties of tholins depend on their chemical composition, and particularly on the

808 N- and O-content. As Pluto tholins are compositionally different from Titan tholins, we propose

809 the optical constants determined in this study as new input parameters from 270 to 2100 nm to

810 model Pluto's atmosphere and surface properties.

811 Our Pluto optical constants were used as input parameters in a Pluto surface model developed

812 by Protopapa et al. (2020). The modelling results concluded on the suitability of our optical

813 constants to reproduce Pluto compositional observations by MVIC and LEISA, at least in the

814 UV-Vis spectral ranges. Moreover, results from a model of light scattering developed by

815 Rannou et al. (1997, 1999) concluded that Pluto tholins absorb 5 to 10 times less than Titan

816 tholins at 500 nm. This lower absorption is consistent with Alice observations of Pluto's haze.

817 Our study focused on Pluto's aerosols formed by photochemistry. However, we remind that an

818 additional process for the formation of aerosols in Pluto's atmosphere was recently proposed

819 by Lavvas et al. (2020) due to ice condensation on photochemical nuclei. In their hypothesis,

820 the first photochemical ice to condense in the upper atmosphere (near ~500 km of altitude)

821 would be HCN. Then, other photochemical gases, such as C_3H_4, C_6H_6 and predominantly C_4H_2,

822 would condense and coat the HCN ice particles formerly formed. Note that, as Pluto's most

823 abundant gaseous photochemical products – C_2H_2, C_2H_4, and C_2H_6 – condense only a few

824 kilometres above the surface (Stern et al. 2017b), they should not take part in the homogeneous

825 coating of HCN particles occurring at higher altitudes. Nevertheless, those C_2 hydrocarbons, as

826 well as CH_3C_2H, are suspected to be subject to heterogeneous adsorption/desorption processes

827 on the ice particles, between 100 and 200 km of altitude above the surface (Krasnopolsky 2020;

828 Luspay-Kuti et al. 2017; Wong et al. 2017), inhibiting the sublimation of the condensed ices.

829 Such condensation of gaseous molecules, resulting in coated photochemical aerosols

830 (Krasnopolsky 2020; Luspay-Kuti et al. 2017; Wong et al. 2017), would occur on preexisting

831 Pluto's aerosols formed by photochemistry, requiring to know their properties as well, as

832 studied in the present work. The differences observed between our data and the *New Horizons*

833 observations could be explained by this contribution of coated aerosols. By analogy with the

834 C_4H_2 ice studied in Lavvas et al. (2020) presenting lower n- and k-values than those determined

for our Pluto tholins in the common wavelength range [270-1000 nm], we can suppose that if gaseous molecules condense or adsorb on Pluto's photochemical aerosols, their optical constants n and k could be slightly lowered.

However, assessing the exact effect on the optical constants of [tholins/ices] mixture will require in depth modelling and experimental investigation, far beyond the scope of this study.

References

Alcouffe, G., Cavarroc, M., Cernogora, G., et al. 2010, Plasma Sources Sci Technol, 19, 15008, http://dx.doi.org/10.1088/0963-0252/19/1/015008

Azzam, R. M. A., & Bashara, N. M. 1977, Ellipsometry and Polarized Light, Ellipsometry and Polarized Light (North-Holland Publishing Company)

Bertrand, T., & Forget, F. 2016, Nature, 540, 86, https://doi.org/10.1038/nature19337

Bertrand, T., & Forget, F. 2017, Icarus, 287, 72, http://www.sciencedirect.com/science/article/pii/S0019103517300477

863   Bertrand, T., Forget, F., Umurhan, O. M., et al. 2019, Icarus, 329, 148,

864   http://www.sciencedirect.com/science/article/pii/S0019103518305748

865   Bohren, C. F., & Huffman, D. R. 1983, Absorption and Scattering of Light by Small Particles

866   (John Wiley & Sons)

867   Boucher, O. 2015 (Springer Netherlands), https://doi.org/10.1007/978-94-017-9649-1_2

868   Brassé, C., Muñoz, O., Coll, P., & Raulin, F. 2015, Planet Space Sci, 109–110, 159,

869   http://www.sciencedirect.com/science/article/pii/S0032063315000471

870   Brossier, J. F., Rodriguez, S., Cornet, T., et al. 2018, J Geophys Res Planets, 123, 1089,

871   https://doi.org/10.1029/2017JE005399

872   Bruggeman, D. A. G. 1935, Ann Phys, 416, 636, https://doi.org/10.1002/andp.19354160705

873   Cable, M. L., Hörst, S. M., Hodyss, R., et al. 2012, Chem Rev, 112, 1882,

874   https://doi.org/10.1021/cr200221x

875   Cappa, C. D., Che, D. L., Kessler, S. H., Kroll, J. H., & Wilson, K. R. 2011, J Geophys Res

876   Atmos, 116, https://doi.org/10.1029/2011JD015918

877   Carrasco, N., Tigrine, S., Gavilan, L., Nahon, L., & Gudipati, M. S. 2018, Nat Astron, 2, 489,

878   https://doi.org/10.1038/s41550-018-0439-7

879   Cechalova, B., Branecky, M., Klapetek, P., & Cech, V. 2019, Materials, Vol. 12

880   Cheng, A. F., Summers, M. E., Gladstone, G. R., et al. 2017, Icarus, 290, 112,

881   http://www.sciencedirect.com/science/article/pii/S0019103516303141

882   Cheng, A. F., Weaver, H. A., Conard, S. J., et al. 2008, Space Sci Rev, 140, 189,

883   https://doi.org/10.1007/s11214-007-9271-6

884   D'Amico, K. L., Manos, C., & Christensen, R. L. 1980, J Am Chem Soc, 102, 1777,

885   https://doi.org/10.1021/ja00526a003

886   Desyaterik, Y., Sun, Y., Shen, X., et al. 2013, J Geophys Res Atmos, 118, 7389,

887   https://doi.org/10.1002/jgrd.50561

888   Fan, S., Shemansky, D. E., Li, C., et al. 2019, Earth Sp Sci, 6, 1057,

889   https://doi.org/10.1029/2018EA000477

890   Ferrari, A. C., Rodil, S. E., & Robertson, J. 2003, Phys Rev B - Condens Matter Mater Phys,

67, 155306

Fujiwara, H. 2007, Spectroscopic Ellipsometry: Principles and Applications, Spectroscopic
Ellipsometry: Principles and Applications (John Wiley)

Gao, P., Fan, S., Wong, M. L., et al. 2017, Icarus, 287, 116,
http://www.sciencedirect.com/science/article/pii/S0019103516306170

Gautier, T., Sebree, J. A., Li, X., et al. 2017, Planet Space Sci, 140, 27,
http://www.sciencedirect.com/science/article/pii/S003206331630397X

Gavilan, L., Broch, L., Carrasco, N., Fleury, B., & Vettier, L. 2017, Astrophys J, 848, L5,
http://dx.doi.org/10.3847/2041-8213/aa8cc4

Gladstone, G. R., Pryor, W. R., & Stern, S. A. 2015, Icarus, 246, 279,
http://www.sciencedirect.com/science/article/pii/S0019103514002085

Gladstone, G. R., Stern, S. A., Ennico, K. A., et al. 2016, Science (80-), 351,
http://science.sciencemag.org/content/351/6279/aad8866.abstract

Griffith, C. A., Doose, L., Tomasko, M. G., Penteado, P. F., & See, C. 2012, Icarus, 218, 975,
http://www.sciencedirect.com/science/article/pii/S0019103511004611

Grundy, W. M., Bertrand, T., Binzel, R. P., et al. 2018, Icarus, 314, 232,
http://www.sciencedirect.com/science/article/pii/S0019103517306012

Hadamcik, E., Renard, J.-B., Alcouffe, G., et al. 2009, Planet Space Sci, 57, 1631,
http://www.sciencedirect.com/science/article/pii/S0032063309001834

Imanaka, H., Cruikshank, D. P., Khare, B. N., & McKay, C. P. 2012, Icarus, 218, 247,
http://www.sciencedirect.com/science/article/pii/S0019103511004453

Imanaka, H., Khare, B. N., Elsila, J. E., et al. 2004, Icarus, 168, 344,
http://www.sciencedirect.com/science/article/pii/S0019103504000041

Jellison, G. E. J., & Modine, F. A. 1996, Appl Phys Lett, 69, 371,
https://doi.org/10.1063/1.118064

Johnson, P. E., Young, L. A., Protopapa, S., et al. 2021, Icarus, 356, 114070,
http://www.sciencedirect.com/science/article/pii/S0019103520304188

Jovanović, L., Gautier, T., Vuitton, V., et al. 2020, Icarus, 346, 113774,

919   https://doi.org/10.1016/j.icarus.2020.113774

920   Keita, A.-S., En Naciri, A., Delachat, F., et al. 2010, J Appl Phys, 107, 93516,

921   https://doi.org/10.1063/1.3331551

922   Khare, B. N., Sagan, C., Arakawa, E. T., et al. 1984, Icarus, 60, 127,

923   http://www.sciencedirect.com/science/article/pii/0019103584901428

924   Khare, B. N., Sagan, C., Thompson, W. R., Arakawa, E. T., & Votaw, P. 1987, J Geophys

925   Res Sp Phys, 92, 15067, https://doi.org/10.1029/JA092iA13p15067

926   Kolokolova, L., & Jockers, K. 1997, Planet Space Sci, 45, 1543,

927   http://www.sciencedirect.com/science/article/pii/S0032063397000998

928   Kolokolova, L., Jockers, K., Chernova, G. P., & Kiselev, N. N. 1997, Icarus, 126, 351,

929   http://www.sciencedirect.com/science/article/pii/S0019103596956602

930   Kramers, H. A. 1927, in Atti. Cong. Intern. Fisica (Transactions of Volta Centenary

931   Congress) Como 2, 545

932   Krasnopolsky, V. A. 2020, Icarus, 335, 113374,

933   http://www.sciencedirect.com/science/article/pii/S0019103519302313

934   van Krevelen, D. W., & te Nijenhuis, K. 2009, in Properties of Polymers - Fourth edition,

935   287, http://www.sciencedirect.com/science/article/pii/B9780444828774500172

936   Kronig, R. de L. 1926, J Opt Soc Am, 12, 547,

937   http://www.osapublishing.org/abstract.cfm?URI=josa-12-6-547

938   Lambe, A. T., Cappa, C. D., Massoli, P., et al. 2013, Environ Sci Technol, 47, 6349,

939   https://doi.org/10.1021/es401043j

940   Larson, E. J. L., Toon, O. B., West, R. A., & Friedson, A. J. 2015, Icarus, 254, 122,

941   http://www.sciencedirect.com/science/article/pii/S0019103515001104

942   Lavvas, P., Lellouch, E., Strobel, D. F., et al. 2020, Nat Astron,

943   https://doi.org/10.1038/s41550-020-01270-3

944   Lavvas, P., Strobel, D. F., Lellouch, E., et al. 2016, in AAS/Division for Planetary Sciences

945   Meeting Abstracts #48, 224.06, https://ui.adsabs.harvard.edu/abs/2016DPS....4822406L

946   Lavvas, P., Yelle, R. V., & Griffith, C. A. 2010, Icarus, 210, 832,

947   http://www.sciencedirect.com/science/article/pii/S0019103510003040

948   Lavvas, P., Yelle, R. V., & Vuitton, V. 2009, Icarus, 201, 626,

949   http://www.sciencedirect.com/science/article/pii/S0019103509000086

950   Lellouch, E., Gurwell, M. A., Butler, B. J., et al. 2017, Icarus, 286, 289,

951   http://www.sciencedirect.com/science/article/pii/S0019103516302755

952   Liang, M.-C., Yung, Y. L., & Shemansky, D. E. 2007, Astrophys J, 661, L199,

953   http://dx.doi.org/10.1086/518785

954   Likhachev, D. V., Malkova, N., & Poslavsky, L. 2015, Thin Solid Films, 589, 844,

955   http://www.sciencedirect.com/science/article/pii/S0040609015007014

956   Liu, P. F., Abdelmalki, N., Hung, H.-M., et al. 2015, Atmos Chem Phys, 15, 1435,

957   https://ui.adsabs.harvard.edu/abs/2015ACP....15.1435L

958   Lopes, R. M. C., Malaska, M. J., Solomonidou, A., et al. 2016, Icarus, 270, 162,

959   http://www.sciencedirect.com/science/article/pii/S0019103515005576

960   Luspay-Kuti, A., Mandt, K. E., Jessup, K. L., et al. 2017, Mon Not R Astron Soc, 472, 104

961   Mahjoub, A., Carrasco, N., Dahoo, P.-R., et al. 2012, Icarus, 221, 670,

962   http://www.sciencedirect.com/science/article/pii/S001910351200334X

963   Mahjoub, A., Carrasco, N., Dahoo, P.-R., et al. 2014, Plasma Process Polym, 11, 409,

964   https://doi.org/10.1002/ppap.201300150

965   Maillard, J., Carrasco, N., Schmitz-Afonso, I., Gautier, T., & Afonso, C. 2018, Earth Planet

966   Sci Lett, 495, 185, http://www.sciencedirect.com/science/article/pii/S0012821X18302851

967   Mistrik, J., Kasap, S., Ruda, H. E., Koughia, C., & Singh, J. 2017 (Springer International

968   Publishing), https://doi.org/10.1007/978-3-319-48933-9_3

969   Moise, T., Flores, J. M., & Rudich, Y. 2015, Chem Rev, 115, 4400,

970   https://doi.org/10.1021/cr5005259

971   Nakayama, T., Sato, K., Imamura, T., & Matsumi, Y. 2018, Environ Sci Technol, 52, 2566,

972   https://doi.org/10.1021/acs.est.7b05852

973   Nakayama, T., Sato, K., Matsumi, Y., et al. 2012, SOLA, 8, 119

974   Pernot, P., Carrasco, N., Thissen, R., & Schmitz-Afonso, I. 2010, Anal Chem, 82, 1371,

975   https://doi.org/10.1021/ac902458q

976   Protopapa, S., Grundy, W. M., Reuter, D. C., et al. 2017, Icarus, 287, 218,

977   http://www.sciencedirect.com/science/article/pii/S0019103516307692

978   Protopapa, S., Olkin, C. B., Grundy, W. M., et al. 2020, Astron J, 159, 74,

979   http://dx.doi.org/10.3847/1538-3881/ab5e82

980   Quirico, E., Montagnac, G., Lees, V., et al. 2008, Icarus, 198, 218,

981   http://www.sciencedirect.com/science/article/pii/S0019103508002819

982   Ramírez, S. I., Coll, P., da Silva, A., et al. 2002, Icarus, 156, 515,

983   http://www.sciencedirect.com/science/article/pii/S0019103501967831

984   Rannou, P., Cabane, M., Botet, R., & Chassefière, E. 1997, J Geophys Res Planets, 102,

985   10997, https://doi.org/10.1029/97JE00719

986   Rannou, P., Cours, T., Le Mouélic, S., et al. 2010, Icarus, 208, 850,

987   http://www.sciencedirect.com/science/article/pii/S0019103510001181

988   Rannou, P., McKay, C. P., Botet, R. S., & Cabane, M. 1999, Planet Space Sci, 47, 385,

989   http://www.sciencedirect.com/science/article/pii/S0032063399000070

990   Rao, C. N. R. 1975 (Butterworth)

991   Reuter, D. C., Stern, S. A., Scherrer, J., et al. 2008, Space Sci Rev, 140, 129,

992   https://doi.org/10.1007/s11214-008-9375-7

993   Scattergood, T., & Owen, T. 1977, Icarus, 30, 780,

994   http://www.sciencedirect.com/science/article/pii/0019103577900951

995   Sciamma-O'Brien, E., Dahoo, P.-R., Hadamcik, E., et al. 2012, Icarus, 218, 356,

996   http://www.sciencedirect.com/science/article/pii/S0019103511004878

997   Seignovert, B., Rannou, P., Lavvas, P., Cours, T., & West, R. A. 2017, Icarus, 292, 13,

998   http://www.sciencedirect.com/science/article/pii/S0019103516306911

999   Steffl, A. J., Young, L. A., Strobel, D. F., et al. 2020, Astrophys J

1000   Stenberg, B., Viscarra Rossel, R. A., Mouazen, A. M., & Wetterlind, J. 2010, in Advances in

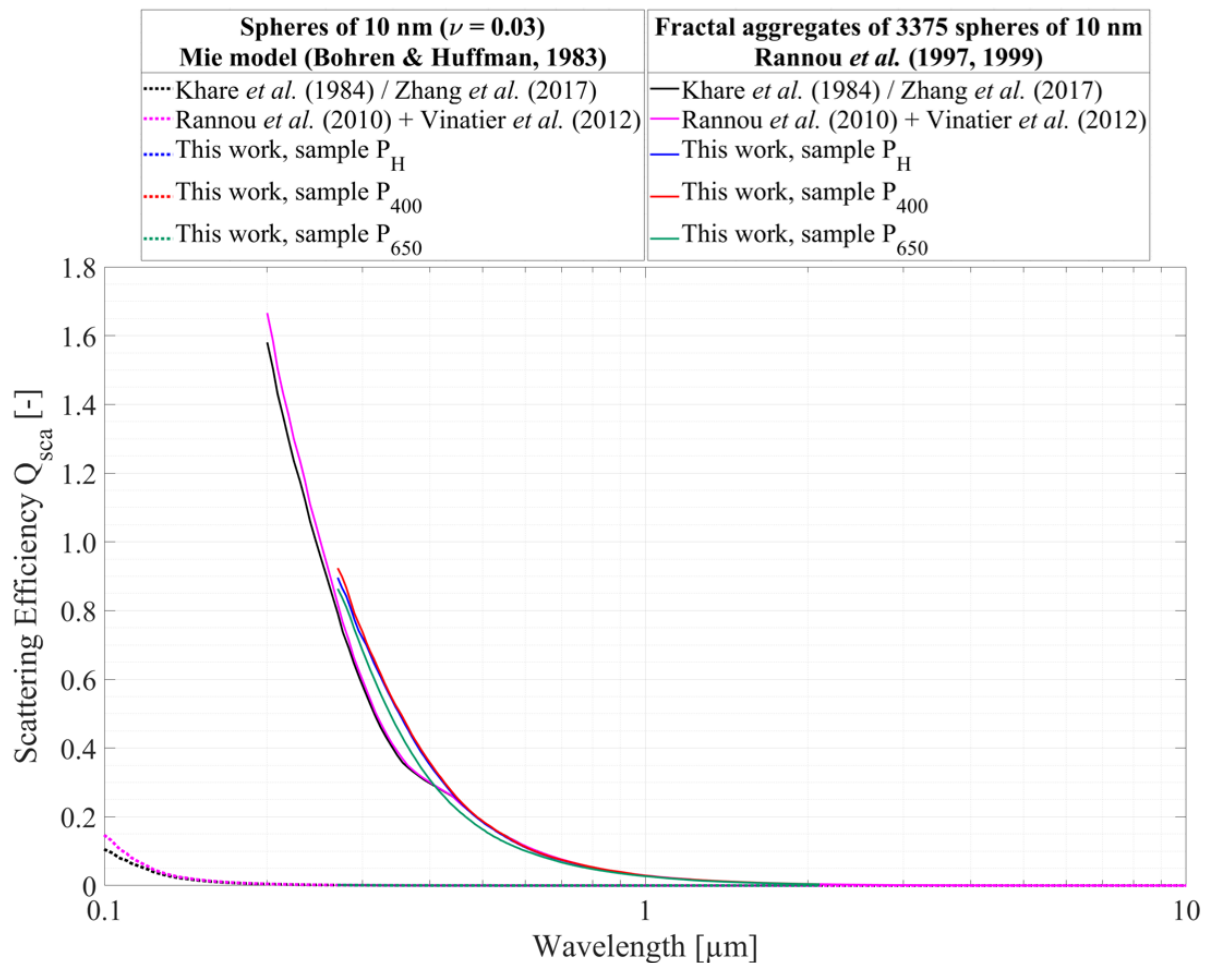1001   Agronomy, ed. D. L. B. T.-A. in A. Sparks, Vol. 107 (Academic Press), 163,

1002   http://www.sciencedirect.com/science/article/pii/S0065211310070057

1003   Stern, S. A., Bagenal, F., Ennico, K. A., et al. 2015, Science (80-), 350,

1004   http://science.sciencemag.org/content/350/6258/aad1815.abstract

1005   Stern, S. A., Binzel, R. P., Earle, A. M., et al. 2017a, Icarus, 287, 47,

1006   http://www.sciencedirect.com/science/article/pii/S0019103516307588

1007   Stern, S. A., Grundy, W. M., McKinnon, W. B., Weaver, H. A., & Young, L. A. 2018, Annu

1008   Rev Astron Astrophys, 56, 357, https://doi.org/10.1146/annurev-astro-081817-051935

1009   Stern, S. A., Kammer, J. A., Barth, E. L., et al. 2017b, Astron J, 154, 43,

1010   http://dx.doi.org/10.3847/1538-3881/aa78ec

1011   Stern, S. A., Slater, D. C., Scherrer, J., et al. 2008, Space Sci Rev, 140, 155,

1012   https://doi.org/10.1007/s11214-008-9407-3

1013   Szopa, C., Cernogora, G., Boufendi, L., Correia, J.-J., & Coll, P. 2006, Planet Space Sci, 54,

1014   394, http://www.sciencedirect.com/science/article/pii/S003206330600002X

1015   Tauc, J., Grigorovici, R., & Vancu, A. 1966, Phys Status Solidi, 15, 627,

1016   https://doi.org/10.1002/pssb.19660150224

1017   Tompkins, H. G., & Irene, E. A. 2005, Handbook of Ellipsometry (William Andrew

1018   Publishing)

1019   Tran, B. N., Joseph, J. C., Ferris, J. P., Persans, P. D., & Chera, J. J. 2003, Icarus, 165, 379,

1020   http://www.sciencedirect.com/science/article/pii/S0019103503002094

1021   Vinatier, S., Rannou, P., Anderson, C. M., et al. 2012, Icarus, 219, 5,

1022   http://www.sciencedirect.com/science/article/pii/S0019103512000498

1023   Vuitton, V., Tran, B. N., Persans, P. D., & Ferris, J. P. 2009, Icarus, 203, 663,

1024   http://www.sciencedirect.com/science/article/pii/S0019103509001754

1025   Wong, M. L., Fan, S., Gao, P., et al. 2017, Icarus, 287, 110,

1026   http://www.sciencedirect.com/science/article/pii/S0019103516306145

1027   Workman, J., & Weyer, L. 2008, Practical Guide to Interpretive Near-Infrared Spectroscopy,

1028   Vol. 3

1029   Xiaobo, Z., Jiewen, Z., Povey, M. J. W., Holmes, M., & Hanpin, M. 2010, Anal Chim Acta,

1030   667, 14, http://www.sciencedirect.com/science/article/pii/S0003267010003582

1031   Young, L. A., Kammer, J. A., Steffl, A. J., et al. 2018, Icarus, 300, 174,

1032   http://www.sciencedirect.com/science/article/pii/S0019103517302609

1033   Zhang, X., Strobel, D. F., & Imanaka, H. 2017, Nature, 551, 352,

1034   https://doi.org/10.1038/nature24465

1035   Zhong, M., Jang, M., Oliferenko, A., Pillai, G. G., & Katritzky, A. R. 2012, Phys Chem Chem

1036   Phys, 14, 9058, http://dx.doi.org/10.1039/C2CP23906J

1037   Zhu, X., Strobel, D. F., & Erwin, J. T. 2014, Icarus, 228, 301,

1038   http://www.sciencedirect.com/science/article/pii/S0019103513004302

1039

1040   **Supplementary Information**

1041

1042

1043   Figure A: Scattering efficiency Q_{sca} determined for spherical monomers of 10 nm radius (log-

1044   normal distribution, with effective variance $\nu = 0.03$) with a Mie model formalized in Bohren

1045 & Huffman (1983) (dotted curves) and for fractal aggregates of 3375 monomers of 10 nm radius

1046 with the model developed by Rannou et al. (1997, 1999) (plain curves). The black curves were

1047 generated with the optical constants determined by Khare et al. (1984) for Titan tholins. Note

1048 that these Khare et al. (1984) optical constants were adopted in Zhang et al. (2017) study. The

1049 pink curves were generated with the optical constants determined by Rannou et al. (2010) and

1050 Vinatier et al. (2012) for Titan's aerosols. The blue, red and green curves were generated with

1051 the optical constants determined respectively for our samples P_H, P_{400} and P_{650}.
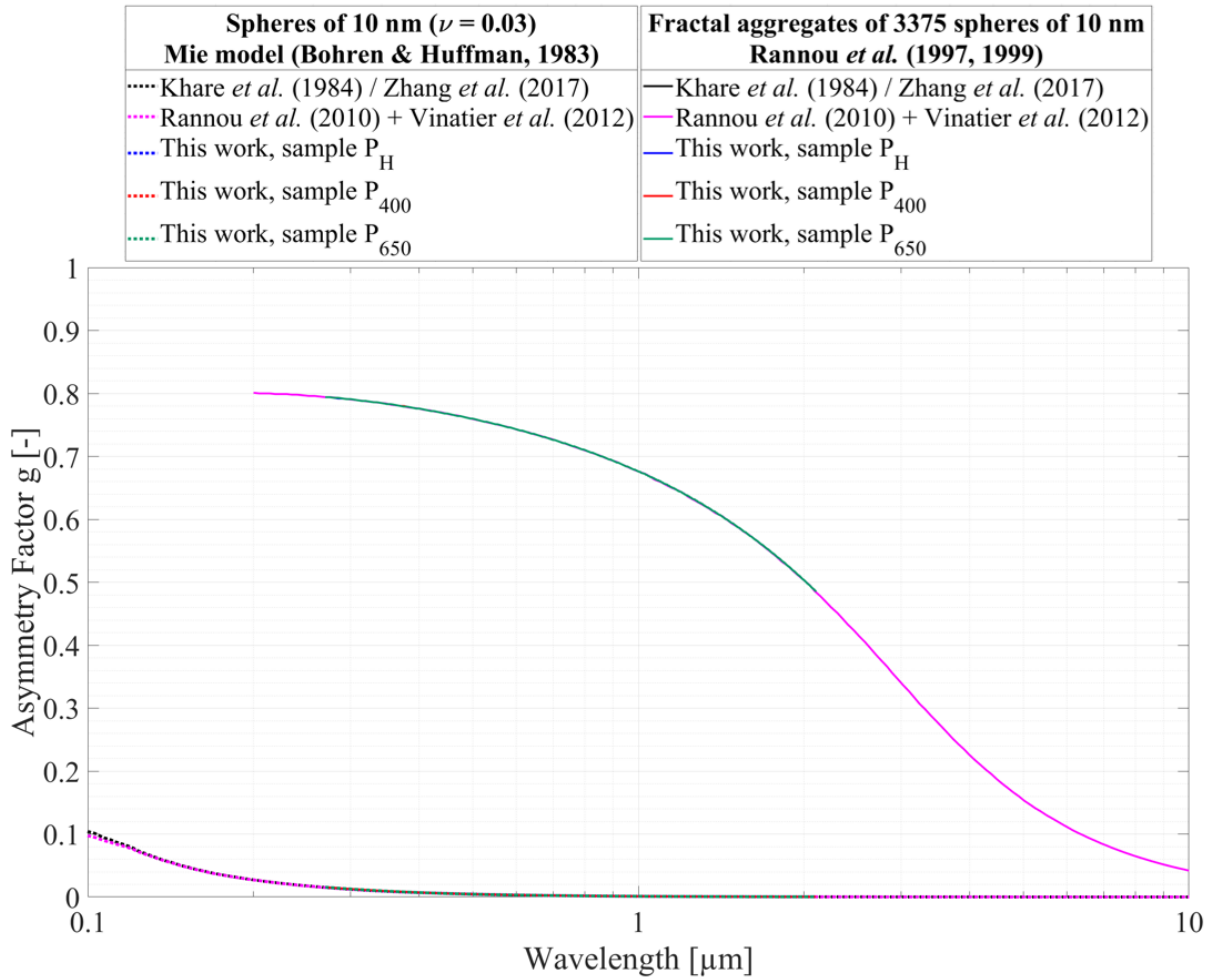

1052

1053 Figure B: Asymmetry factor g determined for spherical monomers of 10 nm radius (log-normal

1054 distribution, with effective variance $\nu = 0.03$) with a Mie model formalized in Bohren &

1055 Huffman (1983) (dotted curves) and for fractal aggregates of 3375 monomers of 10 nm radius

1056 with the model developed by Rannou et al. (1997, 1999) (plain curves). The black curves were

1057 generated with the optical constants determined by Khare et al. (1984) for Titan tholins. Note

1058 that these Khare et al. (1984) optical constants were adopted in Zhang et al. (2017) study. The

1059 pink curves were generated with the optical constants determined by Rannou et al. (2010) and

1060   Vinatier et al. (2012) for Titan's aerosols. The blue, red and green curves were generated with

1061   the optical constants determined respectively for our samples P_H, P_{400} and P_{650}.